Remote Sensing of Environment 233 (2019) 111367

Contents lists available at ScienceDirect

Remote Sensing of Environment

journal homepage: www.elsevier.com/locate/rse

Using overlapping VIIRS scenes to observe short term variations in particulate matter in the coastal environment

Marco Bracaglia[a,b,*], Gianluca Volpe[a], Simone Colella[a], Rosalia Santoleri[a], Federica Braga[c], Vittorio Ernesto Brando[a]

[a] Istituto di Scienze Marine (CNR-ISMAR), Via Fosso del Cavaliere 100, 00133 Rome, Italy
[b] Università degli Studi di Napoli Parthenope, Via Amm. F. Acton 38, 80133 Naples, Italy
[c] Istituto di Scienze Marine (CNR-ISMAR), Arsenale-Tesa 104, Castello 2737/F, 30122 Venice, Italy

ARTICLE INFO

Keywords:
Ocean colour
Particulate backscattering
Coastal environment
Short time variability
Adriatic Sea
VIIRS
Multiple daily observations
Quasi analytical algorithm

ABSTRACT

In coastal areas, the concentrations and the optical properties of the water components have a large spatial and temporal variability, due to river discharges and meteo-marine conditions, such as wind, wave and current, and their interaction with shallow water bathymetry. This large temporal variability cannot be captured using the standard Ocean Colour Radiometry (OCR) polar orbiting satellites, the latter providing almost one image per day. On the contrary, the use of OCR geostationary sensors, like the Geostationary Ocean Colour Imager (GOCI), centred above the Korean Peninsula, enable to capture the short-term variability of the optical properties. To compensate the lack of a geostationary sensor similar to GOCI over other coastal environments, like the North Adriatic Sea (NAS), the multiple observations provided during the same day by the Visible Infrared Imaging Radiometer Suite (VIIRS) mounted on the SUOMI NPP satellite, can be exploited. Indeed, due to its large swath of 3060 km, the VIIRS orbits can overlap over the NAS during the same day within 1 h and 42 min, an important feature that can be useful in capturing the short term variability of the optical properties.

A large number of VIIRS overlaps in the NAS are characterized by high sensor zenith angle (SZA) of the observation, resulting in a large portion of images masked by the high satellite zenith flag. In order to make available those observations and, in general, to reduce the dependence of the VIIRS observations from the SZA, an adjustment based on a multi linear regression scheme, which exploits radiometric in situ observations, was here applied.

This study aims to prove the suitability of the adjusted overlapping VIIRS in capturing the short time scale dynamics of particulate backscattering, and this was demonstrated by the analysis of a case study for the 21st and 22nd of March 2013. In order to evaluate the advantages in using multiple observations during the same day, also the ~24 h dynamics was analysed, comparing the overlapping VIIRS results with the ones obtained from the daily product.

1. Introduction

The concentrations and optical properties of the water components in coastal areas are strongly influenced by the short-term effects of river discharges, meteo-marine conditions and their interaction with shallow bathymetry, that can be more evident than long-term effects (Blondeau-Patissier et al., 2009; Degobbis et al., 2000; Manzo et al., 2018). These forcings and their interaction have a large impact on the geophysical and biogeochemical processes, like coastal erosion and eutrophication events (Collins and Balson, 2007; Duan et al., 2014; Ganju et al., 2014). To support the monitoring of such processes, accurate satellite estimates of inherent optical properties (IOPs), like particulate backscattering (b_{bp}), and absorption from non-algal particulate and dissolved matter (a_{dg}) at high spatial and temporal resolution are needed, due to their large variability in the coastal areas (Babin et al., 2003a; Babin et al., 2003b; Blondeau-Patissier et al., 2009). Indeed, from the spectra of remote sensing reflectance (R_{rs}), retrieved from satellite sensors, it is possible to evaluate the IOPs of the water constituents, using appropriate algorithms (e.g Brando et al., 2012; Lee et al., 2002; Werdell et al., 2013; Werdell et al., 2018).

Several works have successfully used satellite Ocean Colour Radiometry (OCR) data, retrieved from sensors like the Moderate-

* Corresponding author at: Istituto di Scienze Marine (CNR-ISMAR), Via Fosso del Cavaliere 100, 00133 Roma, Italy.
E-mail address: marco.bracaglia@artov.ismar.cnr.it (M. Bracaglia).

https://doi.org/10.1016/j.rse.2019.111367
Received 19 February 2019; Received in revised form 19 July 2019; Accepted 9 August 2019

Resolution Imaging Spectroradiometer (MODIS) and the Sea-Viewing Wide Field-of-View Sensor (SeaWiFS), to capture the seasonal and inter-annual variability, the shape, and the magnitude of the river plumes and their impact on coastal processes (e.g.; Bignami et al., 2007; Dogliotti et al., 2016; Falcini et al., 2012; Fernández-Nóvoa et al., 2017; Le et al., 2013; Schroeder et al., 2012).

In some recent works, the data from sensors like the Multi Spectral Instrument (MSI) on Sentinel2, and the Operational Land Imager (OLI) on Landsat8 have been used to capture the small scales spatial variability of turbidity, chlorophyll and Suspended Particulate Matter (SPM) in the coastal areas (e.g. Braga et al., 2017; Brando et al., 2015; Gernez et al., 2017). Those instruments have a fine spatial resolution (10–60 m), higher than the standard OCR ones (300 m–1000 m), but as they have been designed for land applications, their spectral and radiometric resolutions are not sufficiently accurate to retrieve all the OCR products (Drusch et al., 2012; Pahlevan et al., 2016a; Roy et al., 2014). Moreover, they have smaller temporal resolution (1 image each 5 days or more) than the almost daily one, typical of the OCR polar-orbiting satellites (Hestir et al., 2015; Mouw et al., 2015), still insufficient to capture the short time scale variability typical of the coastal areas (Mouw et al., 2015).

Sensors mounted on geostationary satellites like the Geostationary Ocean Color Imager (GOCI), centred above the Korean Peninsula (Ryu et al., 2012), can acquire multiple observations during the same day. This sensor has been demonstrated feasible in capturing the short time variability of some optical, biological, and biogeochemical properties like R_{rs}, normalized water-leaving radiance, turbidity, and chlorophyll (e.g. Choi et al., 2012; Choi et al., 2014; Concha et al., 2019; Ruddick et al., 2012; Wang et al., 2014), confirming the need of multiple observations during the same day to adequately analyse geophysical and biogeochemical processes in the coastal areas.

This study focuses on the North Adriatic Sea (NAS), a semi-enclosed basin located in the Mediterranean Sea (MED, Fig. 1), characterized by a large number of rivers (listed in Fig. 1), that can discharge waters with different biogeochemical and optical properties (Solidoro et al., 2009). Hence, NAS proves to be a complex system characterized by riverine inputs of different origin, acting in a limited spatial extent, that strongly influence the physical and biogeochemical properties of the basin (Bignami et al., 2007; Marini et al., 2008; Solidoro et al., 2009; Zavatarelli et al., 1998). Between those watercourses, the Po, Adige, and Brenta rivers together provide most of the NAS freshwater (Cozzi and Giani, 2011; Falcieri et al., 2014), but also the effect of the rivers in the Northern part (from Isonzo to Piave, Fig. 1) is relevant for the optical property dynamics (Brando et al., 2015; Marini et al., 2008; Solidoro et al., 2009). Moreover, the wind-driven forcing, especially from Bora and Scirocco, can influence the vertical and horizontal current fields, and, consequently, the sediment transport and the concentration of the water components (Bignami et al., 2007; Harris et al., 2008; Wang and Pinardi, 2002). On the contrary, there is no appreciable net effect of tides on sediment transport and resuspension (Malačič et al., 2000; Wang et al., 2007). Several studies investigated the bio-optical properties and the dynamics of the NAS using in situ and shipboard observations, numerical models, and satellite imagery (e.g. Barale et al., 2008; Boldrin et al., 2009; Loisel et al., 2001).

One geostationary sensor, active over this basin, is the Spinning Enhanced Visible and InfraRed Imager (SEVIRI), mounted on the Meteosat Second Generation (SGM) satellite, designed mainly for meteorological and weather applications (Schmid, 2000). Nevertheless, using the 635 nm SEVIRI spectral band is possible to retrieve turbidity and SPM (Neukermans et al., 2009; Neukermans et al., 2012), but the low radiometric and spectral resolutions prevent the estimation of other OCR products. Moreover, due to its coarse resolution in the NAS area (~6 km) (Ruddick et al., 2014), the instrument cannot detect the small spatial variability, typical of the coastal areas.

In order to obtain multiple observations of the NAS area during the same day, the OCR data provided by the Visible Infrared Imaging Radiometer Suite (VIIRS), mounted on the polar-orbiting satellite SUOMI-NPP (Cao et al., 2013), can be exploited, as suggested by

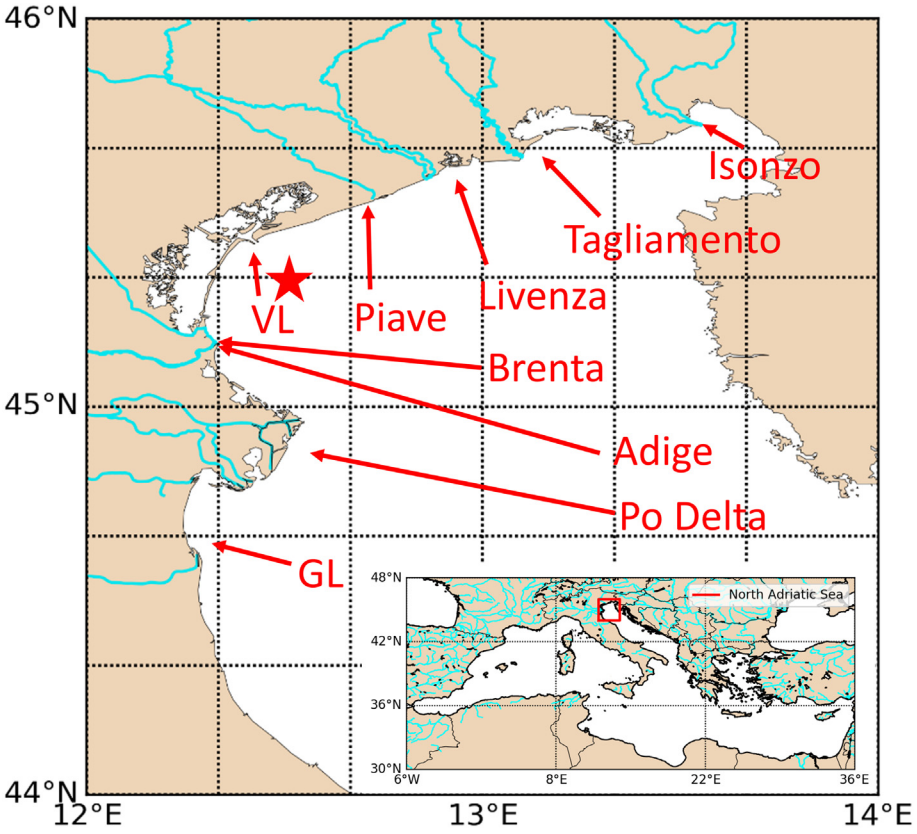

Fig. 1. Map of the NAS with the rivers of the basin. The red star identifies the Acqua Alta Oceanographic Tower (AAOT), VL the Venice Lagoon, and GL the Goro Lagoon. In the box on the bottom right the Mediterranean Sea, with the NAS identified by the red square. (For interpretation of the references to colour in this figure legend, the reader is referred to the web version of this article.)

Arnone et al. (2017). Indeed, in comparison with other OCR polar-orbiting satellites, it has a very large swath (3060 km), with a spatial resolution of 750 m (Cao et al., 2013), and, above the NAS, its orbits can overlap during the same day within 1 h and 42 min (Arnone et al., 2017).

As most of the VIIRS overlaps are characterized by observations performed at sensor zenith angles (SZA) > 60°, those data are generally masked by the High Satellite Zenith (HSZ) flag (NASA 2019), and thus the use of the overlapping VIIRS is hampered. Moreover, Barnes and Hu (2016) demonstrated, comparing data from different satellite sensors, that also the data, not masked by the HSZ flag, show larger differences between each other for higher SZA (Barnes and Hu, 2016), for uncertainties in the normalization of the Water Leaving Radiance (Eplee et al., 2012; Morel et al., 1996; Morel et al., 2002; Morel and Mueller, 2002).

This work aims to analyse the suitability of the overlapping VIIRS in capturing the short time variability ($\Delta t = 102$ min) of b_{bp} at 443 nm ($b_{bp}(443)$), calculated using the quasi analytical algorithm (QAA, Lee et al., 2002; Lee et al., 2014). Moreover, the overlapping VIIRS will be exploited also to analyse the ~24 h variability, comparing the results with those obtained from the Copernicus Marine Environment Monitoring System (CMEMS) multi-sensor daily data (Volpe et al., 2019).

To reduce the uncertainties of the VIIRS R_{rs}, needed as input to calculate $b_{bp}(443)$, to use data generally masked by HSZ flag, and to reduce the SZA dependence of the VIIRS observations, the Acqua Alta Oceanographic Tower (AAOT) in situ radiometric data will be exploited to adjust the VIIRS data, using a multi-linear regression (MLR) scheme (D'Alimonte et al., 2008).

This paper is structured as follows: in the next section, an overview of the VIIRS and in situ instruments and data will be provided. Moreover, the methods used to process and select the satellite images, to calculate the optical parameters, to perform the match-up analysis used to assess the quality of the VIIRS R_{rs} spectra, to adjust the R_{rs} spectra, and to select the case study will be presented.

In Section 3 the results obtained in this work are presented, and the suitability of VIIRS in capturing the $b_{bp}(443)$ short time scale dynamics is demonstrated, presenting the case study for the 21st and 22nd of March 2013. In particular, the advantages of using the overlapping VIIRS single sensor data in comparison with the CMEMS multi-sensor daily data will be discussed.

In Section 4 the obtained results will then be summarized and discussed, and some future perspectives for this work will be presented.

2. Data and methods

2.1. CMEMS

The CMEMS multi-sensor daily product, derived from the merging of inter-bias corrected data from different OC sensors, provides a long time series of OCR data (1997 to date) (Volpe et al., 2019). Starting from the R_{rs} Level 2 (L2) data, provided by different space agencies, the CMEMS operational processing chain makes available various Level 3 (L3) OCR products on a standard equirectangular grid at 1 km resolution (Volpe et al., 2019). For the period of our interest (2012–2018) the CMEMS R_{rs} data are derived from the merging of the VIIRS and MODIS-AQUA (MODIS-A) data.

In the first steps of the CMEMS processing the data from the different sensors are treated separately: in the passage from L2 to L3 single sensor data, some flags are applied (Volpe et al., 2019), to mask data that could be affected by large sources of uncertainties, that can be due to both environmental and instrumental conditions (NASA 2019). After the flag application, the images are destriped (Bouali and Ignatov, 2014; Mikelsons et al., 2014) and the VIIRS bow-tie missing data (Cao et al., 2013) are filled. The destriping method is the one used for the SST data by Bouali and Ignatov (2014) and adapted to R_{rs} data by Mikelsons et al. (2014), while, to fill the VIIRS bowtie deleted pixels a simple linear interpolation is performed (Cao et al., 2013). Then, after some quality checks, a band-shifting, and an inter-bias correction procedure, the single sensor data are reprojected on a common 1kmx1km equirectangular grid and merged together (Volpe et al., 2019).

The CMEMS reflectance data have demonstrated to be accurate and reliable in the NAS, due to their good agreement with the in situ observations (Volpe et al., 2019). The IOPs retrieved from the CMEMS R_{rs} spectra will be here used as reference to compare the results obtained from the overlapping VIIRS data, in order to evaluate the advantages in using multiple observations during the same day in capturing the short time variation of $b_{bp}(443)$ in the basin.

2.2. VIIRS sensor and image pre-processing

The VIIRS sensor is a scanning radiometer, on board of the SUOMI-NPP polar-orbiting satellite. It is located at an altitude of 829 km, with a swath width of 3060 km, and a revisiting time of 16 days (Cao et al., 2013). The instrument has 22 spectral bands in the range 410–12,010 nm, with a spatial resolution that varies between 350 and 750 m (depending on the band) (Cao et al., 2013). For the purpose of our work only the OCR products provided by VIIRS were needed and, consequently, only the data acquired by the OCR bands at 410, 443, 486, 551 and 671 nm, that are characterized by a spatial resolution of 750 m and a bandwidth of 20 nm (18 for 443 nm) (Cao et al., 2013).

In this work, the VIIRS L2 R_{rs} data, retrieved from the NASA with the processing version R2018 (NASA, 2018), were used. In particular, all the VIIRS L2 images, acquired between 2012/01/03 (end of VIIRS commissioning phase) and 2018/08/31, containing observations of the NAS area, were selected and processed implementing most of the CMEMS processing chain for the MED, as listed above (Volpe et al., 2019).

To make available also the data acquired near coastlines and estuaries (Barnes et al., 2019) and more orbit overlaps, the Stray Light (SL) and the HSZ flags were not applied.

- The SL flag masks all the pixels that can be affected by the adjacency effect of clouds and lands. Indeed, for measurements performed over pixels close to the shore, the light reflected by the land surface can be forward scattered into the sensor field of view, and this can result in an abnormal increase of the reflectance in the near-infrared (NIR) (Kaufman, 1984; Sterckx et al., 2011; Van Mol and Ruddick, 2005).
- The HSZ flag masks the pixel corresponding to data acquired at SZA larger than 60° because they can be affected by residuals due to both path radiance in the atmospheric correction and normalization of the water leaving radiance (Morel et al., 2002; Morel and Mueller, 2002).

Then the data were destriped and the bowtie missing data were filled (Bouali and Ignatov, 2014; Cao et al., 2013; Mikelsons et al., 2014), consistently with the CMEMS procedures described in Section 2.1.

Finally, all the images were re-projected on a common 750mx750m equirectangular grid, by a nearest neighbour method using the pyproj and pyresample Python packages (Python 2019; Python 2019b); in such way, it was possible to use the same grid for each image, in order to compare them.

2.3. In situ data at Acqua Alta Oceanographic Tower

The AAOT, shown in Fig. 1, is located in the NAS, 8 nautical miles south-east off the Venice Lagoon (12.509° E, 45.314° N). The AAOT is used to continuously collect comprehensive atmospheric and marine coastal measurements. An automated station of the AERONET network (Holben et al., 1998) equipped with a CIMEL sun–sky radiometer instrument is also installed. This network was originally developed to monitor the atmospheric aerosol and to validate satellite products

connected to them (Holben et al., 1998). AAOT is part of the AERONET-OC network, an extension of AERONET, where, besides atmospheric acquisitions, ocean colour measurements are also performed. Indeed, at AAOT, in addition to the standard network observations, also water leaving radiance is measured by the SeaWiFS Photometer Revision for Incident Surface Measurements (SeaPRISM), which provides measurements of the sky and sea radiance at different view and azimuth angles and eight different wavelengths between 412 and 1020 nm (Zibordi et al., 2006; Zibordi et al., 2009a).

The AERONET-OC data are available for download (NASA 2019b) with three processing levels: L1 are unscreened data, L1.5 are cloud screened data and L2 are cloud screened and quality-assured data. In this work, the L2 data, integrated with the L1.5, for periods where the L2 were missing, were exploited to compare and adjust the VIIRS data. In particular, the AAOT version 2 dataset was used; here the ocean colour nominal bands are at 412, 443, 488, 531, 551, and 667 nm, while those at 870 and 1020 nm are used for quality assurance, and turbid water flagging (Zibordi et al., 2009a; Zibordi et al., 2002).

In the AAOT area, the optical properties exhibit a wide variability, indeed waters typical of both off-shore and coastal areas can be observed (Zibordi et al., 2009a). Consequently, in this work, the OCR data, acquired at this location, were considered as representative of the basin variability (Mélin et al., 2011).

2.4. The quasi-analytical algorithm

QAA is an inversion algorithm used to retrieve the IOPs of the water components from remote-sensing observations, using analytical, semi-analytical, and empirical formulations (Lee et al., 2002). Various QAA versions were implemented during the years (e.g. Lee et al., 2002; Lee et al., 2011; Lee et al., 2014); in this study, consistently with CMEMS processing (Section 2.1, Volpe et al., 2019), the QAA version 6 was adopted. The QAA formulations are listed in Table 1 (Lee et al., 2002; Lee et al., 2014). In this model, to retrieve the IOPs of interest, the R_{rs} spectrum is converted into below water R_{rs} (r_{rs}) at step0 of the algorithm, and this quantity is then used to calculate the function u (step1). Then the total absorption (a) and b_{bp} at the reference wavelength (551 or 671 nm, depending on the $R_{rs}(671)$ value) are calculated (steps 2 and 3). From those is possible to evaluate the spectrum of those two IOPs (steps 5 and 6), calculating the b_{bp} spectral slope (η, step4). Subtracting the pure water contribution from the total absorption, this is then decomposed into two components: a_{dg} and the phytoplankton absorption (a_{ph}). At step 9a of the model $a_{dg}(443)$ is evaluated, and then its spectrum and the one for a_{ph} can be retrieved (steps 9b-10), after the a_{dg} spectral slope calculation (S, step 8a).

As the QAA is an algebraic and step-wise algorithm that exploits analytical, semi-analytical and empirical formulations, the input and model uncertainties propagate in the retrieval (Lee et al., 2002; Lee et al., 2010; Lee et al., 2014). In the work of Lee et al. (2010), the propagation of the model uncertainties has been analysed comparing the algorithm outputs with a simulated dataset for different parameters on a wide IOP range. In this analysis, a(551) showed a good agreement with the correspondent simulated quantity for the 0.058–0.4 m^{-1} range, which covers most of the oceanic and coastal waters. The uncertainty of a(551) propagated in the retrieval of $b_{bp}(551)$, showing larger absolute percentage differences. This propagation is more notable in the retrieval of $a_{dg}(443)$, where the largest contribution to the uncertainty is linked to the total absorption in the blue part of the spectrum (a(412) at step9a), while the contribution of ζ and ξ is lower.

In Lee et al. (2010), to evaluate only the uncertainty propagation due to the model assumptions and formulations, the uncertainty associated to the input R_{rs} spectra and to steps 0 and 1 was set to 0. In this study, in Section 3.1.2 the effect of the uncertainty associated to VIIRS R_{rs} on the retrieval of IOP amplitude and shape factors will be evaluated.

2.5. Match-up analysis

As previously mentioned, data acquired at high SZA can have large sources of uncertainties (Barnes and Hu, 2016). Hence, to assess the quality of the VIIRS R_{rs} spectra, a pairwise match-up analysis with the AAOT in situ data was performed.

In this analysis, for each VIIRS image, the AAOT data acquired in temporal proximity ($\Delta t < 30$ min) with the VIIRS observations (t_{VIIRS}) were selected. The acquisition time of the VIIRS observation was calculated starting from the value of msec (milliseconds of the day) in the VIIRS L2 file, for the pixel collocated with AAOT. The Δt was chosen equal to 30 min to ensure that the same in situ data were not used for two overlapping orbits during the same day and to take into account the short time variability of the R_{rs} spectra. For what concerns the satellite

Table 1
List of all the steps of QAA v6 (Lee et al., 2011). h0, h1 and h2 are three constants. b_{bw} and a_w are the contribution of the water to backscattering and absorption.

Step	Formula
0	$r_{rs}(\lambda) = R_{rs}(\lambda)(0.52 + 1.7R_{rs}(\lambda))$
1	$u(\lambda) = \frac{-g_0 + \sqrt{g_0^2 + 4g_1 r_{rs}(\lambda)}}{2g_1}$ *with* $g_0 = 0.089$ $g_1 = 0.1245$
	if $r_{rs}(671) < 0.0015\ sr^{-1} \rightarrow \lambda_0 = 551\ nm$ else $\rightarrow \lambda_0 = 671\ nm$
2	$\chi = \log\left(\frac{r_{rs}(443) + r_{rs}(486)}{r_{rs}(551) + 5\frac{r_{rs}(671)}{r_{rs}(486)} r_{rs}(671)}\right)$ $a(\lambda_0) = a_w(\lambda_0) + 0.39\left(\frac{R_{rs}(671)}{R_{rs}(443) + R_{rs}(486)}\right)^{1.14}$
	$a(\lambda_0) = a_w(\lambda_0) + 10^{h0 + h1\chi + h2\chi^2}$
3	$b_{bp}(\lambda_0) = \frac{u(\lambda_0)a(\lambda_0)}{1 - u(\lambda_0)} - b_{bw}(\lambda_0)$
4	$\eta = 2.0\left(1 - 1.2\exp\left(-0.9\frac{r_{rs}(443)}{r_{rs}(551)}\right)\right)$
5	$b_{bp}(\lambda) = b_{bp}(\lambda_0)\left(\frac{\lambda_0}{\lambda}\right)^{\eta}$
6	$a(\lambda) = (1 - u(\lambda))(b_{bw}(\lambda) + b_{bp}(\lambda))/u(\lambda)$
7	$\zeta = 0.74 + \frac{0.2}{0.8 + r_{rs}(443)/r_{rs}(551)}$
8a	$S = 0.015 + \frac{0.002}{0.6 + r_{rs}(443)/r_{rs}(551)}$
8b	$\xi = \exp(S(442.5 - 415.5))$
9a	$a_{dg}(443) = \frac{a(412) - \zeta a(443)}{\xi - \zeta} - \frac{a_w(412) - \zeta a_w(443)}{\xi - \zeta}$
9b	$a_{dg}(\lambda) = a_g(443)\exp(-S(\lambda - 443))$
10	$a_{ph}(\lambda) = a(\lambda) - a_{dg}(\lambda) - a_w(\lambda)$

data, a 3 × 3 pixel box around the AAOT location was used for comparison, but only in correspondence of at least 3 valid pixels. The value of the in situ R_{rs} is the mean of all the AAOT data acquired between t_{VIIRS}-Δt and t_{VIIRS} + Δt, while the value of the VIIRS R_{rs} is the mean of the 3 × 3 box data.

Since SeaPRISM has a different set of bands than VIIRS, a band-shifting procedure was applied to the SeaPRISM data towards VIIRS (Zibordi et al., 2009b). The method here applied is the one presented in Mélin and Sclep (2015), which consists in the application of the QAA in the forward and backward modes. Indeed, starting from the native SeaPRISM bands it is possible, using the QAA, to evaluate the IOPs at the VIIRS target wavelengths; then, applying the QAA in forward mode the R_{rs} at target wavelengths can be retrieved (Mélin and Sclep, 2015; Volpe et al., 2019). The band-shifting can be applied when the spectral distances between the target and native wavelengths is of a few nm; in the entire AAOT and VIIRS time series, the maximum difference between those bands is around 5 nm, and for such spectral distances the uncertainty of the approach is estimated to be < 5% (Mélin and Sclep, 2015).

In the R_{rs} match-up analysis, the entire dataset (ED) was divided into two subsets: training (TD) and validation dataset (VD). TD includes all the data acquired between 2012/01/02 and 2015/05/31 and it was used to retrieve the coefficients of the adjustment (presented in Section 2.6); VD includes the data acquired between 2015/06/01 and 2018/08/31 and it was used to validate the VIIRS data before and after the adjustment procedure. Those dates have been chosen to have a similar number of match-up for the two datasets (314 for TD, 339 for VD), acquired in similar illumination conditions (similar solar zenith angles).

All the match-up analyses of this work are listed in Table 2, while the formulations of the statistical parameters needed to test the agreement between two datasets are listed in Table 3. A good agreement between two datasets is achieved when the determination coefficient (r^2) is close to 1 and bias, root mean square difference (RMSD), mean absolute difference (MAD), mean percentage difference (MPD), and mean absolute percentage difference (MAPD) are close to 0.

2.6. VIIRS R_{rs} adjustment

Following D'Alimonte et al. (2008), a statistical correction scheme based on a multilinear regression algorithm (MLR) was used to reduce systematic differences between in situ (AAOT data) and remote-sensing measurements (VIIRS data). Particularly, in this study, this was applied to make available the HSZ observations and to reduce the dependence of the VIIRS observations from the SZA.

In this procedure for each match-up between an in situ and a remote-sensing observation $\Delta R_{rs}(\lambda)$ is calculated as:

$$\Delta R_{rs}(\lambda) = R_{rs}^{is}(\lambda) - R_{rs}^{or}(\lambda) \quad (1)$$

where $R_{rs}^{is}(\lambda)$ is the in situ R_{rs} and R_{rs}^{or} is the original VIIRS R_{rs}. The multilinear regression scheme is:

Table 2
List of all the match-up analyses of the study. Those were performed for each band of R_{rs} and various IOPs retrieved from the QAA. The used datasets (VD or ED) are specified in the last column.

Name of the match-up analysis	x	y	Dataset
MUA1	In situ R_{rs}	Original VIIRS R_{rs}	VD
MUA2	In situ R_{rs}	Adjusted VIIRS R_{rs}	VD
MUAQ1	QAA parameters from in situ R_{rs}	QAA parameters from original VIIRS R_{rs}	ED
MUAQ2	QAA parameters from in situ R_{rs}	QAA parameters from adjusted VIIRS R_{rs}	ED

Table 3
Formulations of the statistical parameters used in this study to assess the agreement between two datasets. x and y are referred to Table 2, n is the number of concurrent observations of the match up.

Statistical Parameter	Formulation
Determination coefficient (r^2)	$r^2 = \frac{\sum_{i=1}^{n}(x_i-\bar{x})(y_i-\bar{y})}{\sqrt{\sum_{i=1}^{n}(x_i-\bar{x})^2}\sqrt{\sum_{i=1}^{n}(y_i-\bar{y})^2}}$
Bias	$bias = \bar{y} - \bar{x}$
Root mean squared difference (RMSD)	$RMSD = \sqrt{\frac{\sum_{i=1}^{n}(y_i-x_i)^2}{n}}$
Mean absolute difference (MAD)	$MAD = \frac{\sum_{i=1}^{n}\lvert y_i-x_i\rvert}{n}$
Mean percentage difference (MPD)	$MPD(\%) = \frac{100}{n}\sum_{i=1}^{n}\frac{y_i-x_i}{x_i}$
Mean absolute percentage difference (MAPD)	$MAPD(\%) = \frac{100}{n}\sum_{i=1}^{n}\left\lvert\frac{y_i-x_i}{x_i}\right\rvert$

$$<\Delta R_{rs}(\lambda)> = a_0^{sat} + \sum_{i=1}^{5} a_i^{sat} R_{rs}^{or}(\lambda_i) + a_6^{sat} SZA + a_7^{sat} SOLZ + a_8^{sat} RELA \quad (2)$$

where the input vectors are the original R_{rs} spectra, the SZA, the solar zenith angles (SOLZ), and the relative angles between the sensor and the solar azimuth angles (RELA). SZA, SOLZ, and RELA were extracted from the VIIRS L1 data, downloading the L1 GEO files, from the NASA site (NASA 2019) for all the correspondent L2 file. In the MLR scheme, the value of those geometric parameters is the one correspondent to the pixel collocated with AAOT.

The coefficients a_i^{sat} (i = 0, …,8) were calculated performing an ordinary least squares multi-linear regression (Python 2019) between ΔRrs(λ) and the input vectors. Then the adjusted R_{rs} can be retrieved with:

$$R_{rs}^{adj}(\lambda) = R_{rs}^{or}(\lambda) + <\Delta R_{rs}(\lambda)> \quad (3)$$

The adjusted R_{rs} were then used to calculate b_{bp}(443), using the QAA (Lee et al., 2002; Lee et al., 2014).

2.7. Selection of the case study

In this work, a single two-day case study will be presented in order to prove the suitability of VIIRS in capturing the short time scale dynamics of b_{bp}(443). VIIRS has a revisiting time of 16 days, so each day of the cycle was labelled with a number from 1 to 16, with 2012/01/02 being the day 1 and so on. The days in the 16 day cycle with a full VIIRS overlap above NAS are 1, 2, 3, 6, 7, 8, 11, 12, and 13. Only couples with two consecutive days with a full overlap of the orbits were considered (e.g 1–2, 2–3, 6–7 and so on), in such way it will be possible to analyse, not only the short time variability, but also the ~24 h one, in order to compare the obtained results with those obtained with the CMEMS multi sensor daily product. Also, the river flows were considered in choosing the case study, in order to have at disposal a considerable amount of particulate and dissolved matter carried by the rivers prior to and during our days of interest.

Based on those criteria, the case study of 21st and 22nd March 2013 was selected, corresponding to days 12 and 13 of the VIIRS orbital cycle for which two consecutive overlaps of VIIRS are available. In Fig. 2 the river flow time series for Piave, Livenza, and Po during March 2013 are presented. The data, available for different years, were acquired respectively by ARPA Veneto (ARPAV 2019) at the station of Ponte Piave, and Livenza Meduna and by Arpa Emilia Romagna (ARPAE 2019) at the station of Ponte Lagoscuro. For the first two rivers, chosen as representative of the northern part of the area, a low river flow is observed during the first days of the month; on 17th of March, a minimum is observed, followed by a strong increase, until the peak reached during the 19th of March. After this, a still notable river flow is observed during the 20th of March, but lower than the one observed in the

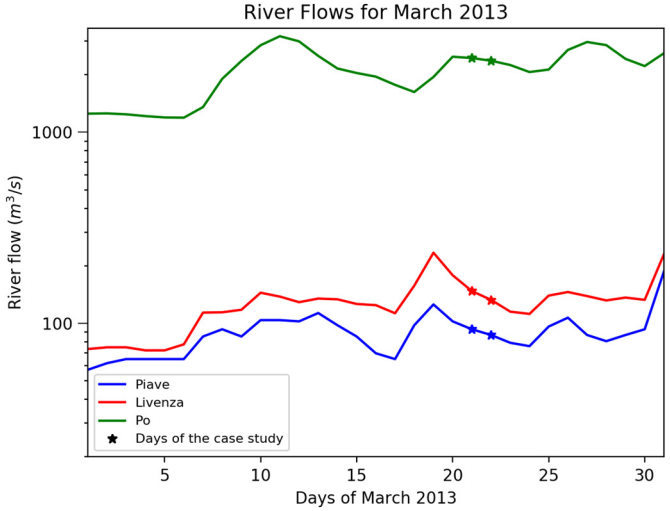

Fig. 2. River flows of Piave, Livenza, and Po during March 2013. On the x axes the day of the month, on the y axes the river flows of the three rivers in the logarithmic scale.

previous day, while the flows continue to decrease in the following days. For Piave, the river flow on the 19th of March (125.6 m^3/s) is the second higher value of the month and for the 20th of March the observed value of 102.4 m^3/s, is still well above the monthly mean of 89.4 m^3/s. For Livenza the river flow measured on 19th of March (234.4 m^3/s) is the maximum observed during the month, while the one observed on 20th of March (178.6 m^3/s) is the third value for this period. For the Po river, the values (1949.4 and 2487.03 m^3/s) are not too high in comparison with the maximum value of month (3185 m^3/s), but they are notably larger than those of the other two rivers and close to the annual mean of 1986.94 m^3/s. Hence, for the high river discharges observed in the previous days, a notable quantity of dissolved and particulate matter carried by the rivers was available in the basin at the beginning of the 21st of March.

In Table 4 the range of SZA and the percentage of HSZ observations for the water pixels of the four scenes (two for each day) are presented; for the first day part of SZA of the second scene (9%) are larger than 60°, while for the first image of the 22nd of March the entire basin have values larger than this threshold. It is important to remark again that pixels with SZA > 60° are generally masked out, so, to examine the case study is fundamental to make those observations available in the analysis.

3. Results

3.1. Match-up analysis

3.1.1. R_{rs}

The match-up analyses between the in situ R_{rs} and the original VD

Table 4
Description of the case study. In the first three columns the day of the orbital cycle, the date, and the start time of the VIIRS acquisition. In the last two columns the range of SZA and the percentage of HSZ observations for the water pixels of the scene.

Day of the VIIRS orbital cycle	Date (YYYY-MM-DD)	Start time (UTC)	Sensor zenith angle (°)	Percentage of HSZ pixels (%)
12	2013-03-21	11:06	48.8–55.0	0
12	2013-03-21	12:48	56.0–60.6	9
13	2013-03-22	10:48	60.3–64.8	100
13	2013-03-22	12:30	40.7–47.7	0

VIIRS R_{rs} (MUA1), and between the in situ R_{rs} and the VD adjusted VIIRS R_{rs} (MUA2), are presented in Fig. 3, and Fig. 4, with the correspondent statistical parameters listed in Table 5, and Table 6. For MUA1 the 486 and 551 nm bands show a good agreement, being the majority of the points close to the 1:1 line, r^2 larger than 0.9, and MAPD of 12.1% and 9.9% respectively. The 410, 443, and 671 nm bands show larger discrepancies with respect to the in situ counterpart, with r^2 of 0.58, 0.81 and 0.90 and MAPD of 31.1%, 22.2%, and 31.2% respectively. For these bands a large number of points are far from the 1:1 line, especially the data retrieved from observations with high SZA (> 50°), showing larger MAPD and RMSD in comparison with those with SZA < 50° (Fig. 5).

To overcome this problem and for the discrepancies observed for the 410, 443, and 671 nm bands, the adjustment introduced in Section 2.6 is applied (D'Alimonte et al., 2008). The coefficients, used to calculate the adjusted VIIRS R_{rs}, were retrieved using the TD VIIRS R_{rs} spectra and the correspondent geometric parameters as input vectors of the MLR scheme (Section 2.6).

After the adjustment (MUA2, Fig. 4), the determination coefficient increases for all the bands, especially for the 410 nm one, and MAD, RMSD, MPD, and MAPD are now closer to zero in the entire spectrum (Table 6). Despite its reduction, the value of MAPD for $R_{rs}(671)$ is still large (25.8%), while RMSD is lower than the other bands. This is due to low magnitude observations ($R_{rs}(671) < 1.5 * 10–3\,sr^{-1}$), that have large MAPD and low RMSD; for those values a low absolute difference can correspond to a notable percentage difference. Indeed, masking for $Rrs(671) < 1.5 * 10^{-3}\,sr^{-1}$ MAPD is reduced to 15.2% and RMSD is increased to $4.8 * 10^{-4}\,sr^{-1}$. After the adjustment, the majority of the points are close to the 1:1 line, with those at high SZA improving the most; indeed, in MUA2 the value of MAPD and RMSD for observations acquired at SZA > 50° are now similar to those acquired at SZA < 50° (Fig. 5).

To analyse the SZA dependence of MUA1 and MUA2 summary statistics, RMSD and MAPD were calculated for different ranges of SZA, with a step of 10° (Fig. 5). RMSD is now reduced in each bin for each band, consistently with the aggregated results shown above. Hence, our adjustment reduced a general bias between the remote sensing and in situ measurements, which is likely due to uncertainties in the absolute calibration of the VIIRS sensor and minimization of atmospheric perturbations (D'Alimonte et al., 2008).

Before the adjustment, the values of MAPD and RMSD (Fig. 5a–c) are notably larger for the two last bins (50° < SZA < 60° and 60 < SZA < 70°), especially for the 410 and 671 nm bands. For example, in MUA1, MAPD for the 410 nm band is between 20% and 30% for bins with SZA < 50°, while > 40% for the remaining two bins; RMSD for the 671 nm band is between $2.0 * 10^{-4}\,sr^{-1}$ and $3.4 * 10^{-4}\,sr^{-1}$ for the first bins and between $4.4 * 10^{-4}\,sr^{-1}$ and $5.6 * 10^{-4}\,sr^{-1}$ for the last two. After the adjustment (Fig. 5b-d), for the 410 nm band MAPD is between 10.2% and 14.1% for SZA < 50° and between 14.0% and 16.6% for SZA > 50°; for the 671 nm band RMSD is now between $1.9 * 10^{-4}\,sr^{-1}$ and $3.2 * 10^{-4}\,sr^{-1}$ for the first bins and between $3.1 * 10^{-4}\,sr^{-1}$ and $3.5 * 10^{-4}\,sr^{-1}$ for the last two. After the adjustment, the values of RMSD and MAPD for SZA > 50° are notably closer to the values observed for SZA < 50°, resulting in a reduced SZA dependence of the VIIRS R_{rs} spectra. Moreover, the values observed for MAPD and RMSD for SZA > 50° in MUA2 are lower than those observed in MUA1 for SZA < 50°. Only MAPD for the third and fourth bins in the 671 nm band are increased, but the correspondent value of RMSD is reduced, due to the low magnitude observations with large MAPD and low RMSD, analysed above. Hence, values previously masked by the HSZ flag can now be made available for our analysis, as their uncertainty is largely reduced.

Our area of interest is only 2° × 2° and in most of the VIIRS overlaps at least one of the two orbits includes observations generally masked from HSZ. Discarding those observations, an almost complete overlap of VIIRS is available for only the day 12 of the orbital cycle and the use of

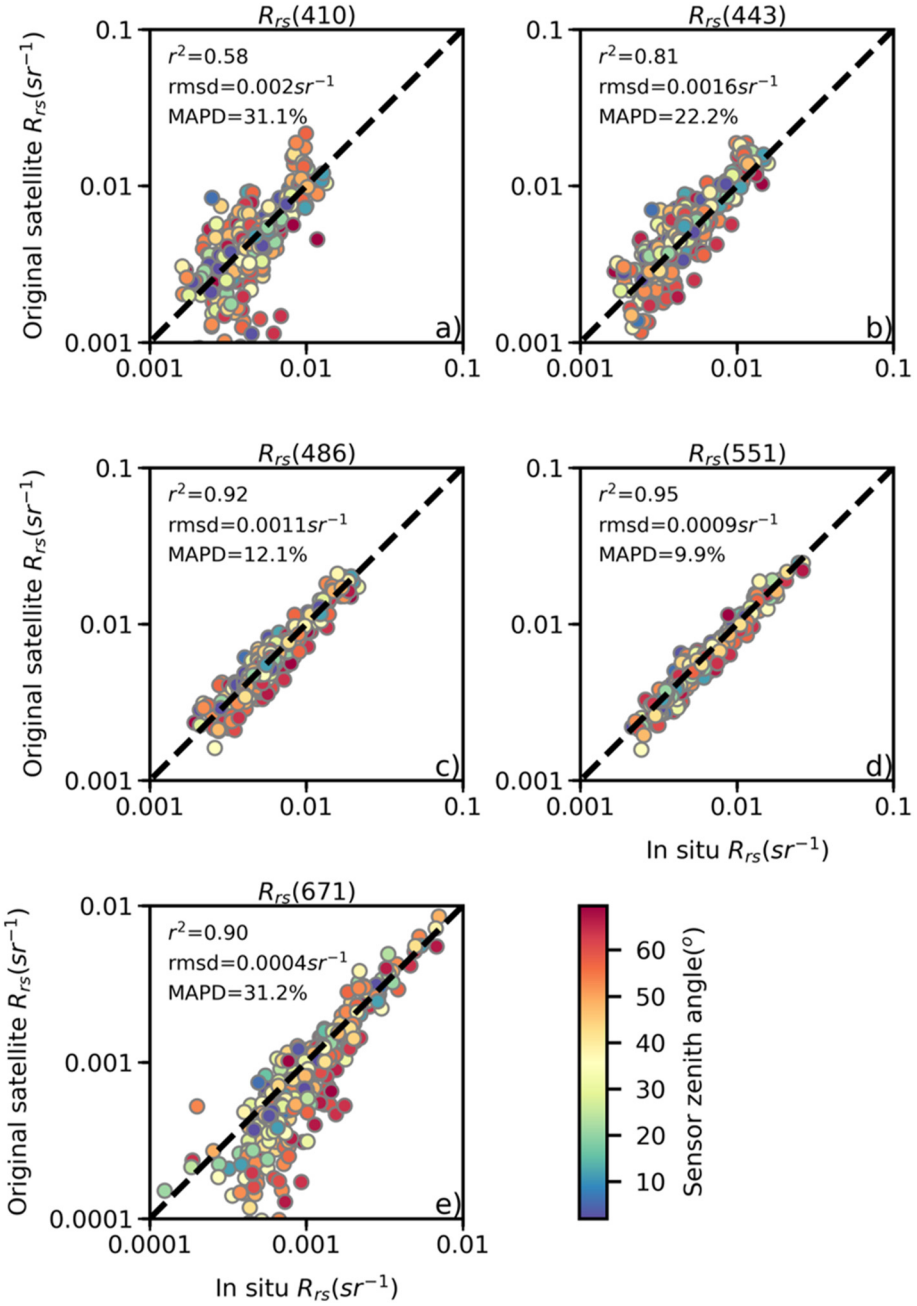

Fig. 3. Match-up analysis between the in situ R_{rs} and the original VD VIIRS R_{rs} (MUA1). In the logarithmic scale on the x axes the in situ R_{rs} and on the y axes the original VIIRS R_{rs}, for each band, with the SZA of the VIIRS observations identified by the colours of the points.

VIIRS in capturing short time scale events in the NAS is, consequently, hampered. On the contrary, the adjustment makes the data previously discarded as reliable as those with SZA $< 50°$. The complete overlap is now available for 9 days in the 16-day cycle (56.3% of total).

Some uncertainties can be introduced by the use of the stray-light affected data and by the linear interpolation performed to make available the bow-tie pixels; nevertheless, the match-up analyses for those adjusted data do not show considerable larger uncertainties in comparison with MUA2 (not shown).

3.1.2. QAA

In this section, the agreement between the QAA parameters retrieved from the in situ R_{rs} and those retrieved from the satellite R_{rs} is evaluated. Then, the effect of the ΔR_{rs} introduced by the adjustment on the retrieval of IOP amplitude and shape factors is analysed. These analyses are not meant to validate the satellite-derived QAA parameters, as also the in situ ones are retrieved by using the same model and, for this reason, the data from ED are used.

In Fig. 6, MUAQ1 is shown, while the MUAQ1 statistical parameters for a(551), $b_{bp}(551)$, η, $b_{bp}(443)$, and $a_{dg}(443)$ are given in Table 5. The calculated a(551) and η show a low determination coefficient, and MAPD of 10.2% and 21.2% respectively, while $b_{bp}(443)$ and $b_{bp}(551)$ show a very similar behaviour with each other and a good agreement with the AAOT QAA parameters (r2 ≥ 0.9, MAPD ~18%, and RMSD respectively of $4.3 * 10^{-3}$ m^{-1} and $5.2 * 10^{-3}$ m^{-1}). On the contrary, there are large discrepancies between the in situ and satellite-derived $a_{dg}(443)$, which shows the lowest value of r^2 and the largest value of MAPD. MUAQ2 is presented in Fig. 7. and the corresponding statistical parameters are given in Table 6. Also in this case, the adjustment improved the agreement between all the parameters, increasing the r^2,

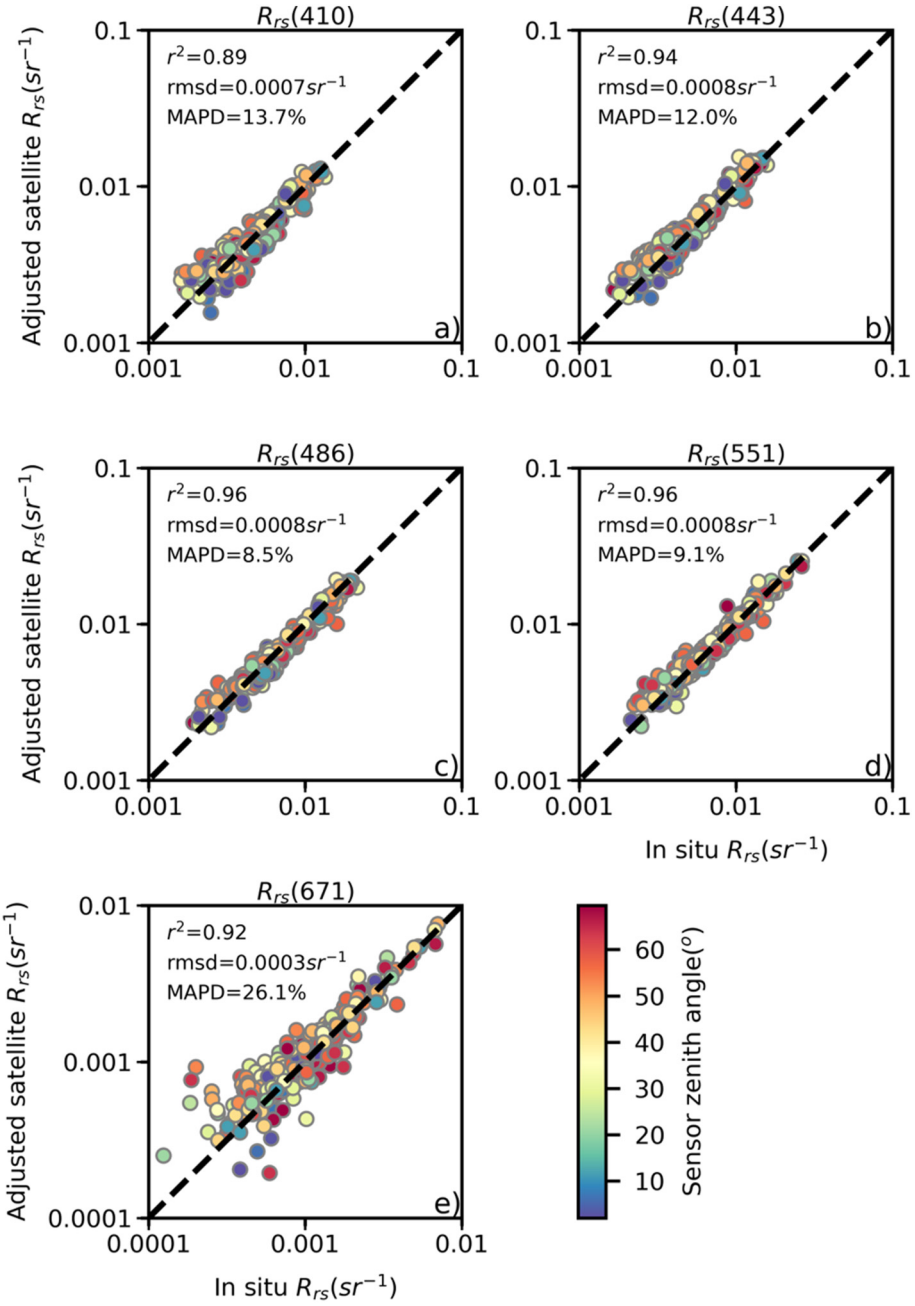

Fig. 4. Match-up analysis between the in situ R_{rs} and the adjusted VD VIIRS R_{rs}. In logarithmic scale on the x axes the in situ R_{rs} and on the y axes the adjusted VIIRS R_{rs}, for each band, with the SZA of the VIIRS observations identified by the colours of the points.

Table 5
Statistical parameters for the match-up analysis between the AAOT in situ R_{rs} and the original VD VIIRS R_{rs} (MUA1) and the QAA-parameters retrieved from the in situ R_{rs} and the original ED VIIRS R_{rs} (MUAQ1).

Product	r^2	Bias	RMSD	MAD	MPD(%)	MAPD(%)
R_{rs} (410)	0.58	$-1.3*10^{-4}\,sr^{-1}$	$2.0*10^{-3}\,sr^{-1}$	$1.4*10^{-3}\,sr^{-1}$	−3.3	31.1
R_{rs} (443)	0.81	$5.5*10^{-4}\,sr^{-1}$	$1.6*10^{-3}\,sr^{-1}$	$1.1*10^{-3}\,sr^{-1}$	10.3	22.2
R_{rs}(486)	0.92	$-1.6*10^{-4}\,sr^{-1}$	$1.1*10^{-3}\,sr^{-1}$	$0.8*10^{-3}\,sr^{-1}$	−2.3	12.1
R_{rs}(551)	0.95	$-3.2*10^{-4}\,sr^{-1}$	$0.9*10^{-3}\,sr^{-1}$	$0.7*10^{-3}\,sr^{-1}$	−4.7	9.9
R_{rs}(671)	0.90	$-1.6*10^{-4}\,sr^{-1}$	$3.9*10^{-4}\,sr^{-1}$	$0.3*10^{-3}\,sr^{-1}$	−21.2	31.2
a(551)	0.66	$-4.8*10^{-3}\,m^{-1}$	$1.78*10^{-2}\,m^{-1}$	$1.1*10^{-2}\,m^{-1}$	−4.3	10.2
b_{bp}(551)	0.91	$-1.2*10^{-3}\,m^{-1}$	$4.3*10^{-3}\,m^{-1}$	$2.7*10^{-3}\,m^{-1}$	−11.4	18.4
η	0.50	$6.5*10^{-2}$	$2.2*10^{-1}$	$1.6*10^{-1}$	8.9	21.2
b_{bp}(443)	0.90	$-1.1*10^{-3}\,m^{-1}$	$5.2*10^{-3}\,m^{-1}$	$3.2*10^{-3}\,m^{-1}$	−9.7	17.9
a_{dg}(443)	0.43	$1.0*10^{-2}\,m^{-1}$	$5.4*10^{-2}\,m^{-1}$	$3.9*10^{-2}\,m^{-1}$	18.7	39.0

Table 6
Statistical parameters for the match-up analysis between the AAOT in situ R_{rs} and the adjusted VD VIIRS R_{rs} (MUA2) and the QAA-parameters retrieved from the in situ R_{rs} and the adjusted ED VIIRS R_{rs} (MUAQ2).

Product	r^2	Bias	RMSD	MAD	MPD(%)	MAPD(%)
$R_{rs}(410)$	0.89	$2.7*10^{-5}\,sr^{-1}$	$7.3*10^{-4}\,sr^{-1}$	$5.7*10^{-4}\,sr^{-1}$	2.7	13.7
$R_{rs}(443)$	0.94	$2.5*10^{-4}\,sr^{-1}$	$7.6*10^{-4}\,sr^{-1}$	$5.5*10^{-4}\,sr^{-1}$	6.8	12.0
$R_{rs}(486)$	0.96	$-1.8*10^{-4}\,sr^{-1}$	$8.2*10^{-4}\,sr^{-1}$	$5.6*10^{-4}\,sr^{-1}$	−0.8	8.5
$R_{rs}(551)$	0.96	$1.8*10^{-4}\,sr^{-1}$	$8.2*10^{-4}\,sr^{-1}$	$5.5*10^{-4}\,sr^{-1}$	4.8	9.1
$R_{rs}(671)$	0.92	$1.0*10^{-4}\,sr^{-1}$	$2.9*10^{-4}\,sr^{-1}$	$2.2*10^{-4}\,sr^{-1}$	17.8	26.1
a(551)	0.78	$4.7*10^{-4}\,m^{-1}$	$1.3*10^{-2}\,m^{-1}$	$7.5*10^{-3}\,m^{-1}$	1.4	6.8
$b_{bp}(551)$	0.92	$2.5*10^{-4}\,m^{-1}$	$3.5*10^{-3}\,m^{-1}$	$2.1*10^{-3}\,m^{-1}$	5.3	14.7
η	0.90	$6.9*10^{-3}$	$7.1*10^{-2}$	$5.5*10^{-2}$	1.7	7.3
$b_{bp}(443)$	0.92	$3.5*10^{-4}\,m^{-1}$	$4.2*10^{-3}\,m^{-1}$	$2.4*10^{-3}\,m^{-1}$	5.4	14.5
$a_{dg}(443)$	0.61	$1.1*10^{-3}\,m^{-1}$	$3.8*10^{-2}\,m^{-1}$	$2.5*10^{-2}\,m^{-1}$	8.2	23.6

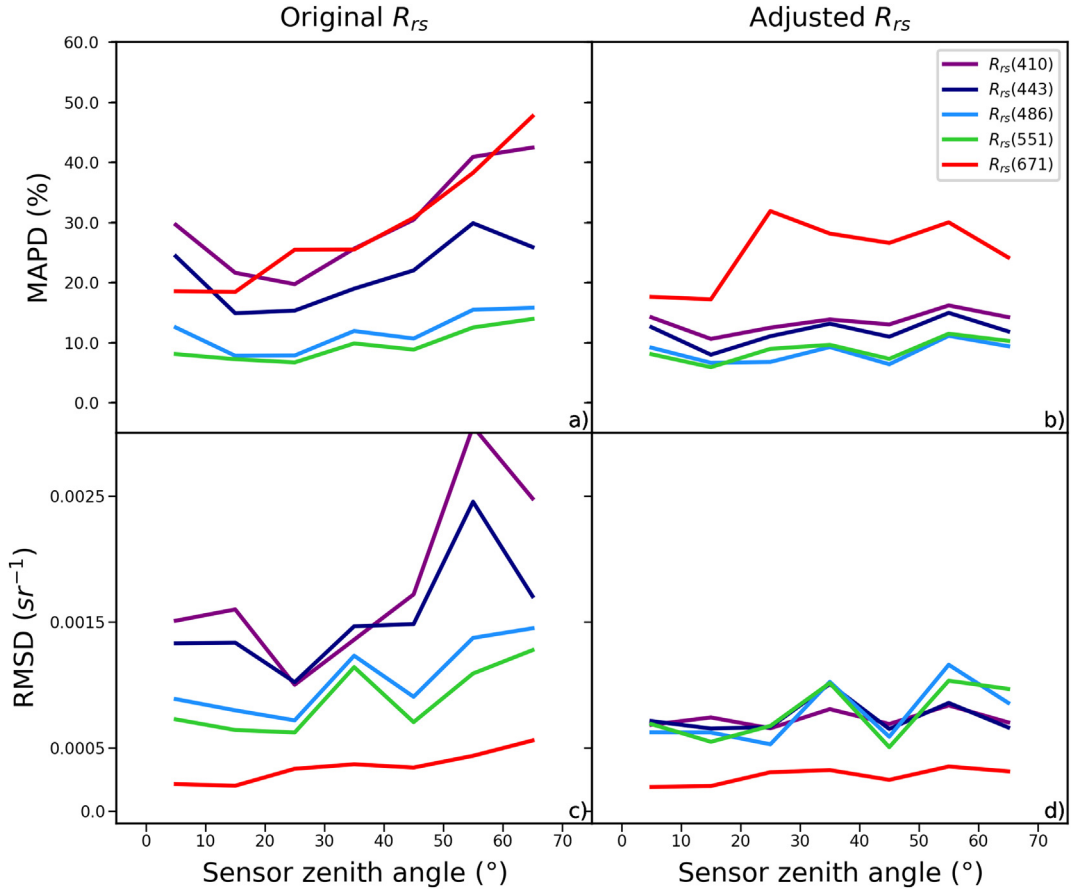

Fig. 5. Analysis of the dependence of the summary statistics from the SZA for MUA1 and MUA2. MAPD (Figure a–b) and RMSD (Figure c–d) were calculated for different ranges of SZA, with a step of 10°.

and decreasing the bias, RMSD, MAD, MPD, and MAPD.

The quality of the QAA outputs is dependent on the input R_{rs} spectrum uncertainty; indeed, the improvement of the MUAQ2 statistics in comparison with MUAQ1 is due to the reduction of the differences between the satellite and in situ spectra (MUA1 and MUA2, Section 3.1.1). The effect of the ΔR_{rs} introduced by the adjustment on the uncertainties of the IOPs is now analysed, using the stepwise nature of the algorithm.

At step 2 of the QAA (Table 1), a(551) depends on all bands, except for $R_{rs}(410)$, but the band ratio strongly reduces the differences observed for the 443 and 671 nm bands (MAPD of 10.2% and 6.8% for MUAQ1 and MUAQ2 respectively). The calculated $b_{bp}(551)$ is dependent on a(551) and the differences observed for the latter one are propagated at step 3, with MAPD of 18.4% and 14.7% for MUAQ1 and MUAQ2 respectively. In this analysis, a(551) and $b_{bp}(551)$ are not always correspondent to $a(\lambda_0)$ and $b_{bp}(\lambda_0)$, because the value of λ_0 depends on the value of $R_{rs}(671)$ (Steps 2 and 3, Table 1). For approximately 80% of the observations of our dataset, λ_0 is equal to 551 nm and, for this reason, in our discussion we focused on 551 nm. Moreover, dividing the dataset into two subsets (one for λ_0 = 551 nm and one for λ_0 = 671 nm), the obtained statistical parameters are nearly the same (results not shown). This is due to the fact that MAPD for the $R_{rs}(671)$ band is strongly reduced for values larger than $1.5*10^{-3}\,sr^{-1}$ (Section 3.1.1), which is also the threshold value for the determination of λ_0.

At step 4, η exhibits a large MAPD (21.2% for MUAQ1), due to its dependence on $R_{rs}(443)$, which shows a MAPD of 22.2% in MUA1 (Table 5); after the adjustment MAPD is reduced to 13.7% and 7.3% for $R_{rs}(443)$ and η respectively. The differences associated with η do not influence too much the $b_{bp}(443)$ retrieval (step 5), which shows a

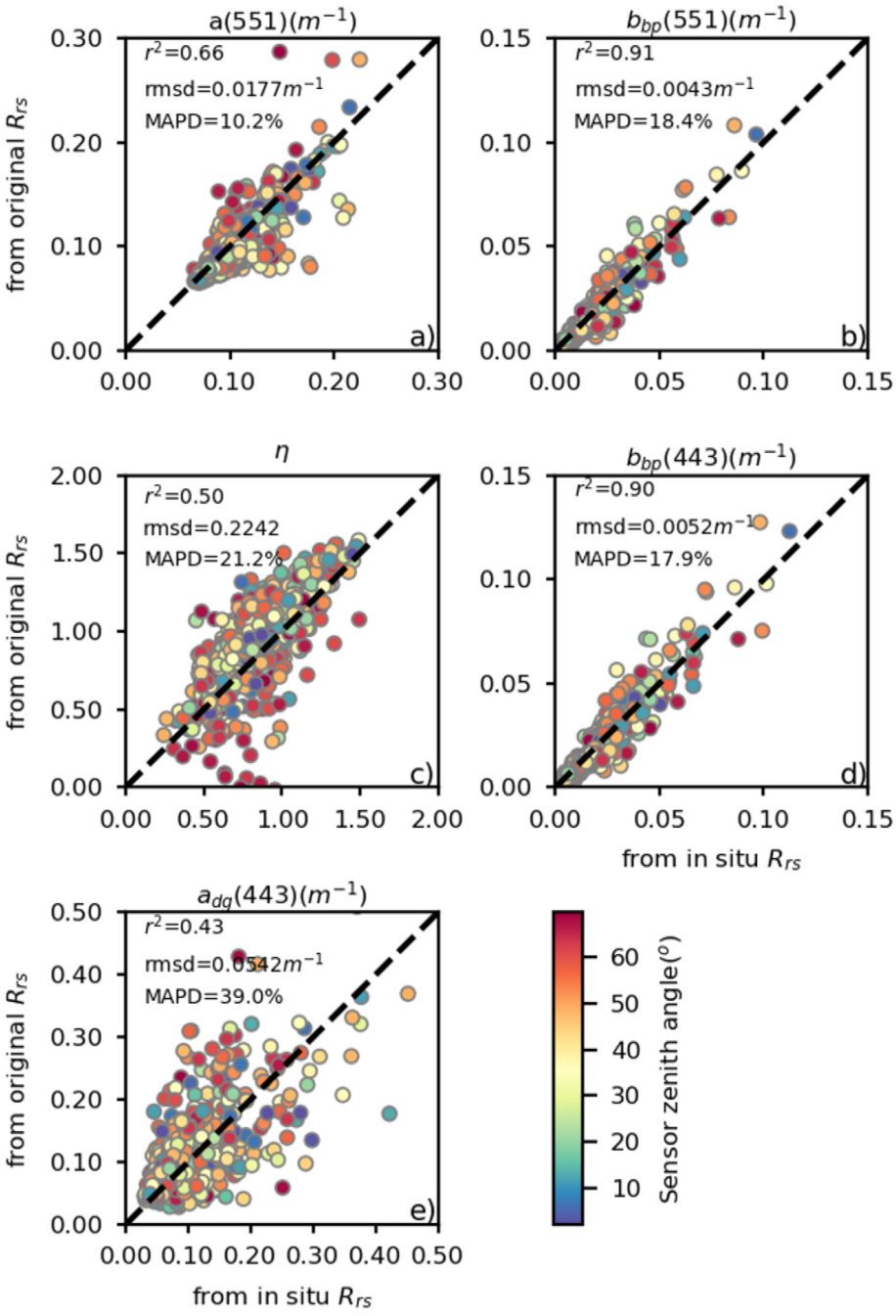

Fig. 6. Match-up analysis between the QAA parameters derived from the in situ R_{rs} and those retrieved from the original ED VIIRS R_{rs}. On the x axis the QAA parameters calculated with the in situ R_{rs}, on the y axis the same parameter calculated with the original VIIRS R_{rs}, with the SZA of the VIIRS observation identified by the different colours of the points.

similar behaviour to $b_{bp}(551)$ in both MUAQ1 and MUAQ2, with MAPD of 17.9% and 14.5% respectively. Finally, at step9a, despite its reduction after the adjustment (from 39.0% to 23.6% from MUAQ1 to MUAQ2), the value of MAPD is still large for $a_{dg}(443)$, while the value of the r^2 of 0.61 in MUAQ2 is still low in comparison with the other IOPs ($r^2 \geq 0.78$).

Our analysis proved that the quality of the $a_{dg}(443)$ calculation can be more sensitive to uncertainties in the retrieval of the R_{rs} spectrum from satellite observations. Indeed, even if the statistic is improved after the adjustment, the uncertainty between the in situ and satellite retrieved $a_{dg}(443)$ is still notable, despite the reduced difference between the two input spectra. As stated earlier, the largest contribution to the $a_{dg}(443)$ uncertainty is linked to the total absorption in the blue part of the spectrum (Section 2.4). The calculated a(412) depends on $R_{rs}(412)$ at step 6 (Table 1), an additional source of uncertainty, which shows the second larger value of MAPD in MUA2; this can strongly influences the quality of the a(412) retrieval and consequently of the $a_{dg}(443)$. These results are consistent with the findings by Wei and Lee (2015), where the QAA derived $a_{dg}(443)$ has been found to have a low r^2 in comparison with the in situ observations. Moreover, the $a_{dg}(443)$ uncertainty is such that when comparing the $a_{dg}(443)$ fields in two overlapping VIIRS acquisitions, it may be difficult to discern between signal and propagated uncertainty in the associated $a_{dg}(443)$ differences. For those reasons, in this study, only the analysis of $b_{bp}(443)$ dynamics will be presented, as the uncertainties of this last parameter are of the same order of those for $b_{bp}(551)$, which has been shown to be

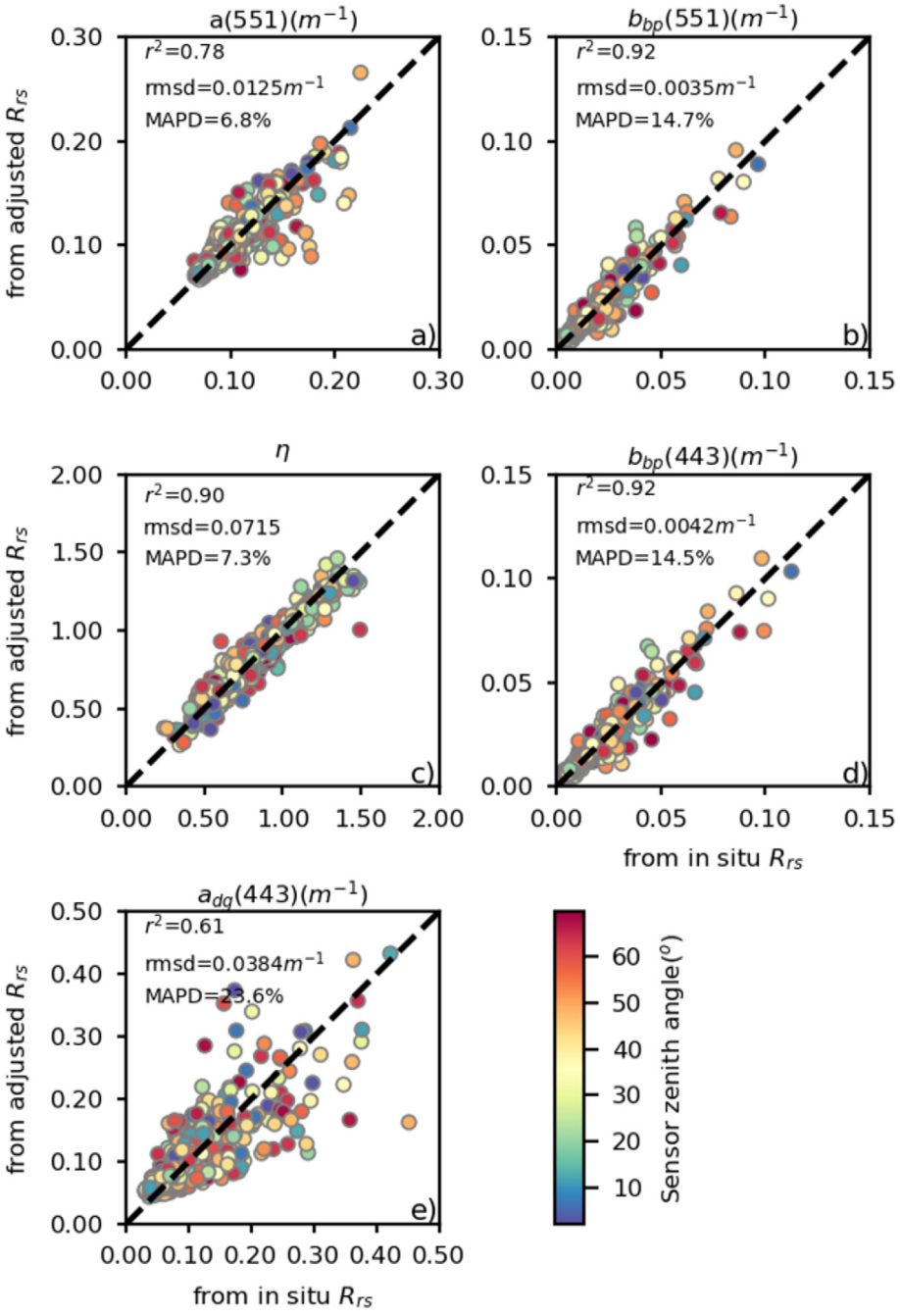

Fig. 7. Match-up analysis between the QAA parameters derived from the in situ R_{rs} and those retrieved from the adjusted ED VIIRS R_{rs}. On the x axis the QAA parameters calculated with the in situ R_{rs}, on the y axis the same parameter calculated with the adjusted VIIRS R_{rs}, with the SZA of the VIIRS observation identified by the different colours of the points.

in good agreement with the situ observations in the NAS (Pitarch et al., 2016).

3.2. Analysis of the case study

3.2.1. CMEMS daily time scale

In Fig. 8 the two maps of CMEMS b_{bp}(443) for the 21st and 22nd March 2013 are shown. After 24 h a general reduction of b_{bp}(443) can be observed in the northern part of the basin, identified by the black isolines (b_{bp}(443) = 0.06 m^{-1}) present in the first map and disappeared in the second one. Nevertheless, due to the daily temporal resolution, it is not possible to understand how and when this reduction took place during the two days. Moreover, the SL flag masks the majority of the pixels near the coastlines and, consequently, information about optical properties cannot be obtained for the pixels closer to the shore. So, the CMEMS multi sensor daily product, due to its temporal resolution and the applied flags, cannot be used to capture the large spatial and temporal variability of the optical properties in the pixels closest to the coast. On the contrary this product can be very useful to analyse the open part of the basin, which is characterized by lower space-time variability, but this is not the aim of this study.

3.2.2. Overlapping VIIRS sub-daily time scale

The adjustment described in 2.5 has been extended to all the NAS area, being AAOT representative of the entire basin (Mélin et al., 2011).

In Fig. 9a–b the adjusted VIIRS b_{bp}(443) maps for the 21st of March

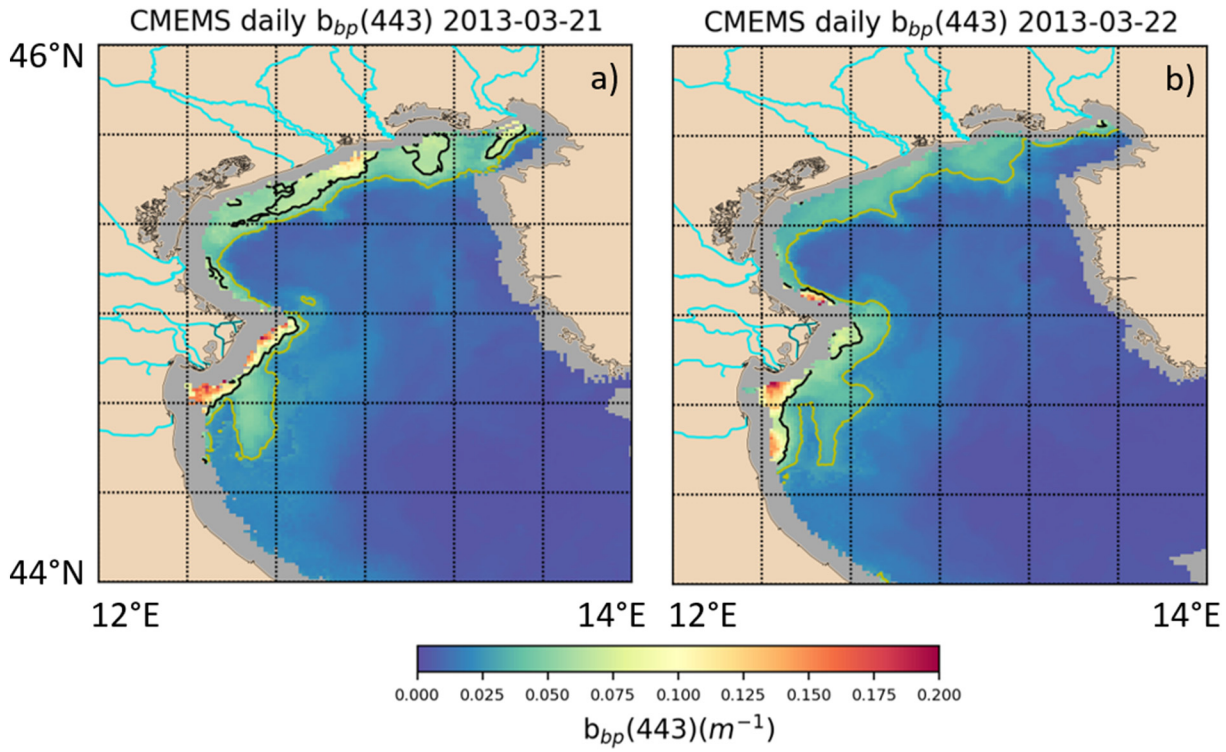

Fig. 8. Maps of the CMEMS $b_{bp}(443)$ product in the NAS for the 21st (a) and 22nd March 2013 (b), with the yellow and black isolines identifying the $b_{bp}(443)$ area respectively of 0.03 m^{-1} and 0.06 m^{-1}. (For interpretation of the references to colour in this figure legend, the reader is referred to the web version of this article.)

(11:06 and 12:48 UTC) are shown. In Fig. 9a large values of $b_{bp}(443)$ can be observed in the entire northern and western coastal area, due to the materials carried by the rivers during the previous days. In this figure, one isoline identifies the plume from the Isonzo river (P1), while the Tagliamento and Livenza plumes create one large area of $b_{bp}(443) = 0.06\ m^{-1}$, which extends westward to the Venice Lagoon (P3). Another structure can be identified between Tagliamento and Isonzo (P2). The area near the Po river mouth is partially masked, but a black isoline (P4) identifies a large structure, which starts from the Brenta and Adige river area and extends southward, also further than the Goro Lagoon. The yellow isoline (P5, $b_{bp}(443) = 0.03\ m^{-1}$) extends in the entire coastal area of the basin at several kilometres from the shore. In the second image of the day (Fig. 9b), after 1 h and 42 m, the main part of P3 does not reach anymore the Venice Lagoon, while the spatial extent of P2 and P1 is consistently reduced. P5 does not shows significant changes in the entire basin, while, in the Po area, a south-eastward shift of P4 is observed. Those changes can be observed in Fig. 9c where the map of $b_{bp}(443)$ difference between the two images of the first day is presented (Fig. 9b minus Fig. 9a), with the isolines from Fig. 9a superimposed. In the northern part, the red area between the black and yellow isolines, where also AAOT is located (Fig. 1), identifies a southward shift of the front; the large blue area inside P5 detects a general reduction of $b_{bp}(443)$, which is more notable in the areas identified by the black isolines, partly dissolved in the second image. The observed differences could be partly due to the uncertainties in satellite data that can be observed between two single satellite images (Qi et al., 2017). Nevertheless, estimating the uncertainties of the satellite observations as the MAD retrieved in MUA2 (Table 6), the differences observed between the two images for each single R_{rs} band (not shown) are above those values for the majority of the coastal pixels. In the same way, estimating the uncertainty of the QAA algorithm in the retrieval of $b_{bp}(443)$ as $2.4 * 10^{-3}\ m^{-1}$ (Table 6) it is possible to argue that the observed differences are not due to artefacts but to realistic processes (Qi et al., 2017).

In Fig. 10 the adjusted VIIRS $b_{bp}(443)$ maps for the 22 of March (10:48 and 12:30 UTC) and the difference between those two are shown. The three isolines (P1, P2, and P3), observed during the first day in the northern part, are almost disappeared while P5 remains very similar to the previous day. The differences between the two images of the day (Fig. 10c) are now very close to zero in the northern area, while some dynamics is still observed in the Western coastal area, with a north-eastward shift of the Po front.

It is important to point out that, in satellite imagery, the data acquired at the edge of a swath are strongly influenced by the pixel growth effect (Cao et al., 2014; Pahlevan et al., 2016b). This is reduced in VIIRS, due to its aggregation algorithm (Cao et al., 2014), but this can be still notable for observations acquired at very large SZA, like the first image of the 22 of March. Indeed this effect can influence the re-projection, based on a nearest neighbour approach, creating some spatial artefacts, as it can be seen in the northern area in Fig. 10a. These spatial artefacts can be more pronounced around fronts, where the sensor could not be able to capture the spatial variability of the area due to the pixel growth effect. For our case study, it is possible to argue that this effect did not provide a misleading determination of the fronts, because in the northern area the differences between the two images, that have different observation geometries (Table 4), are close to zero around fronts.

To analyse the ~24 h dynamics, in Fig. 11a the difference between the two CMEMS images is shown, while in Fig. 11b the difference between the second VIIRS image of the second day and the first VIIRS image of the first day is presented. For the common valid pixels, the two images are very similar, with some differences since the CMEMS product is derived from the merging of the VIIRS and MODIS-A data (Volpe et al., 2019). In Fig. 11a a large portion of coastal pixels have been masked, for the application of the SL flag and, consequently, only the off-shore dynamics can be observed; on the contrary, unmasking the SL flag pixels, in Fig. 11b also the 24 h coastal dynamics can be observed. Moreover, from the previous analysis it is possible to argue that the large reduction of $b_{bp}(443)$ observed in the two last figures is due to a process begun between 11:06 and 12:48 of the 21st of March and

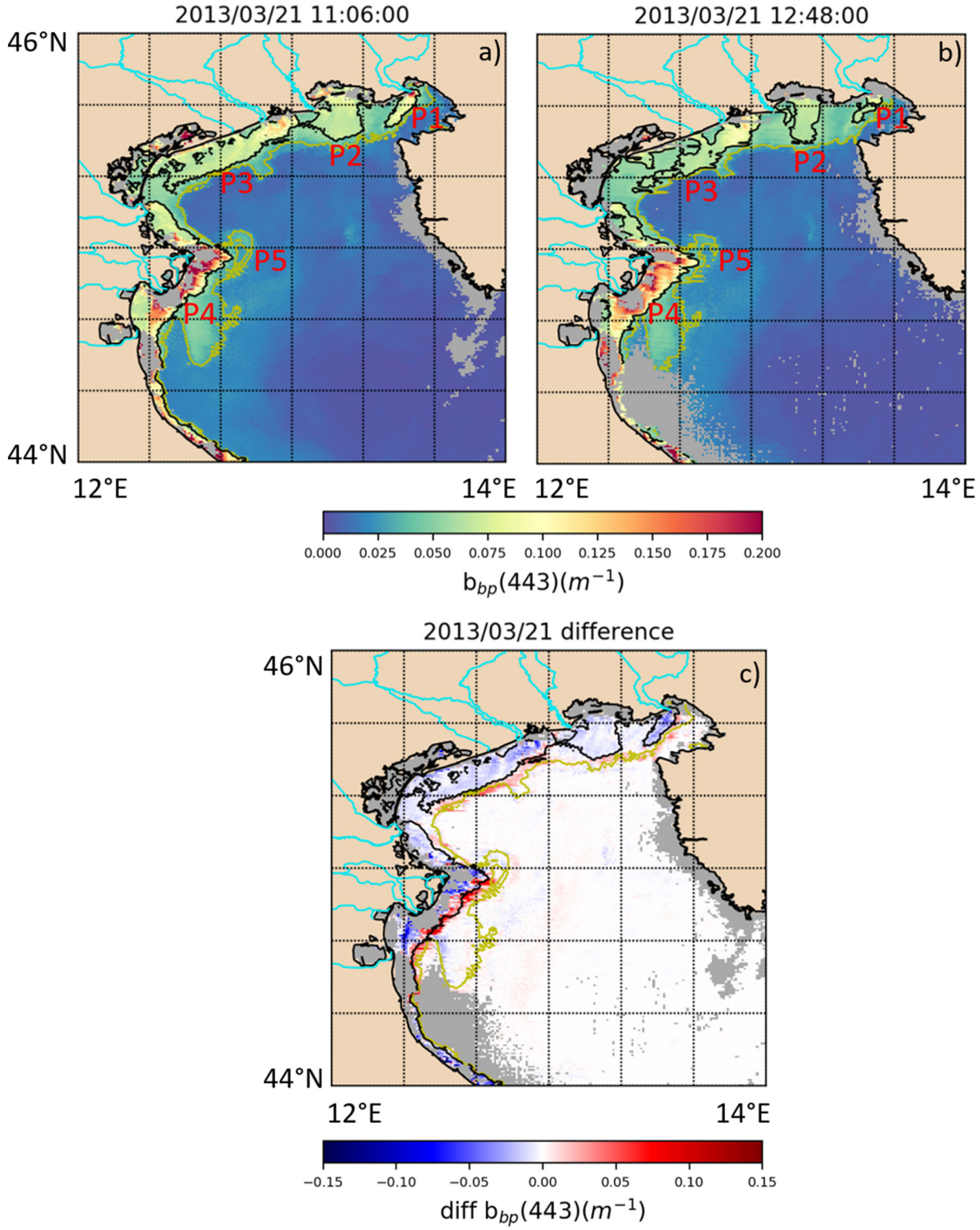

Fig. 9. Analysis of the $b_{bp}(443)$ variability during the 21st of March 2013, derived from the adjusted VIIRS R_{rs}. In a the $b_{bp}(443)$ map at 11:06 UTC, in b the $b_{bp}(443)$ map at 12:48 UTC, in c the map of the difference between the two images (b minus a). The yellow and black isolines identify the $b_{bp}(443)$ area respectively of 0.03 m^{-1} and 0.06 m^{-1}. In figure c the isolines are those from figure a. (For interpretation of the references to colour in this figure legend, the reader is referred to the web version of this article.)

probably most of this reduction has been concentrated during a few hours on the first day, as it can be observed from Fig. 9c.

In order to compare our results with the AAOT $b_{bp}(443)$ dynamics, in Fig. 12 the time series of the in situ, original and adjusted VIIRS $b_{bp}(443)$ is shown.

From the in situ observations an increase of $b_{bp}(443)$ is observed during the morning, confirmed by the southward shift of the front previously observed in Fig. 9c, while between 13 and 15 UTC of 21st of March a large decrease of $b_{bp}(443)$ is observed for the AAOT data. During the second day a lower variability of $b_{bp}(443)$ is observed from

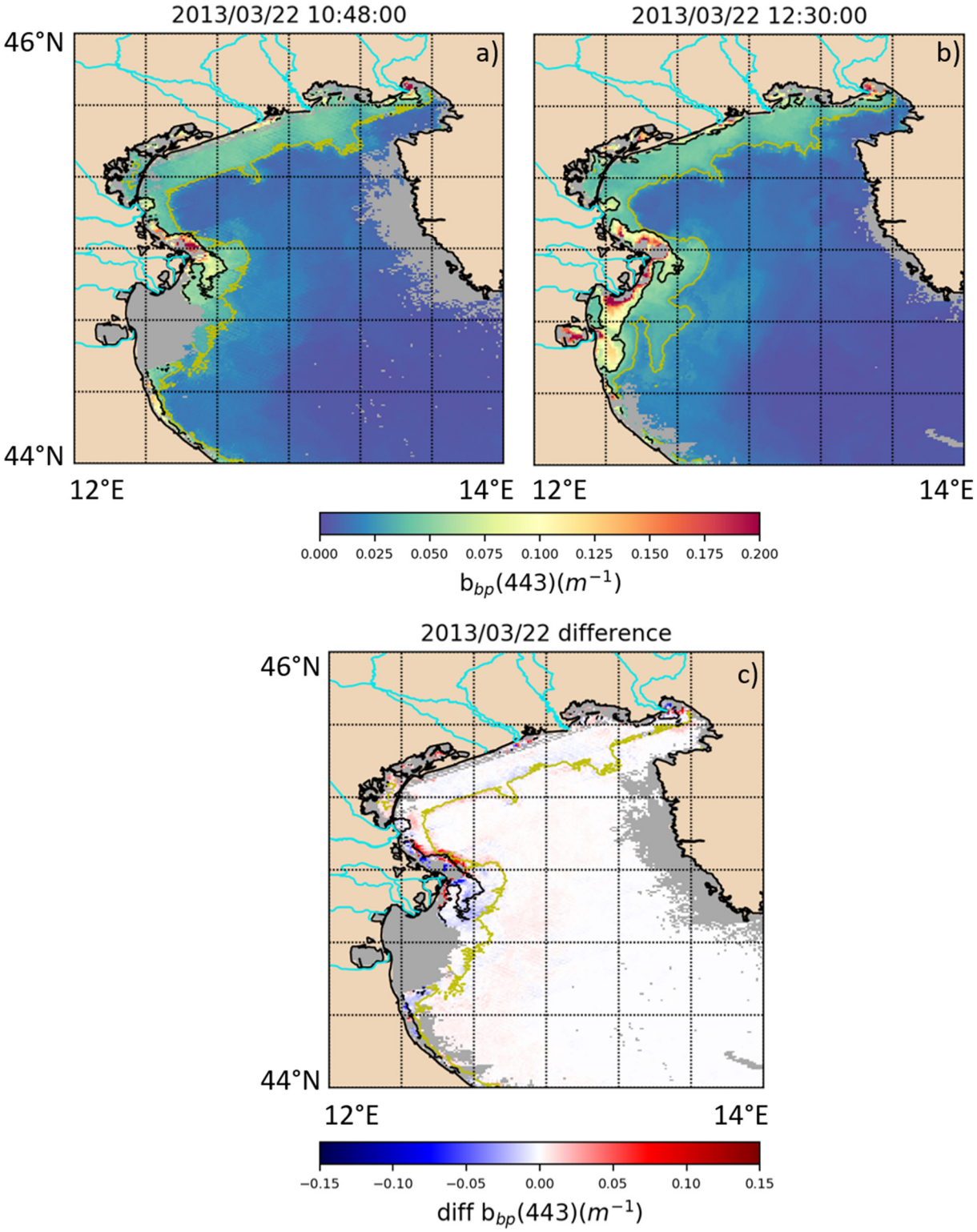

Fig. 10. Analysis of the $b_{bp}(443)$ variability during the 22nd of March 2013, derived from the adjusted VIIRS R_{rs}. In a the $b_{bp}(443)$ map at 10:48 UTC, in b the $b_{bp}(443)$ map at 12:30 UTC, in c the map of the difference between the two images (b minus a). The yellow and black isolines identify the $b_{bp}(443)$ area respectively of 0.03 m^{-1} and 0.06 m^{-1}. In figure c the isolines are those from figure a. (For interpretation of the references to colour in this figure legend, the reader is referred to the web version of this article.)

the in situ data in comparison with the 21st of March, confirming the results of the previous analysis, where great part of the reduction observed between the two days is due to a process which has taken place in a short time range during the first day. Indeed, during the two days, also in the AAOT area a large $b_{bp}(443)$ reduction is observed (Fig. 11b), despite the initial increase detected between the two images on 21st of March.

The adjusted VIIRS observations show a good agreement with the in situ ones, indeed for the second orbit of the two days concurrent AAOT and VIIRS observations are available, showing a percentage difference

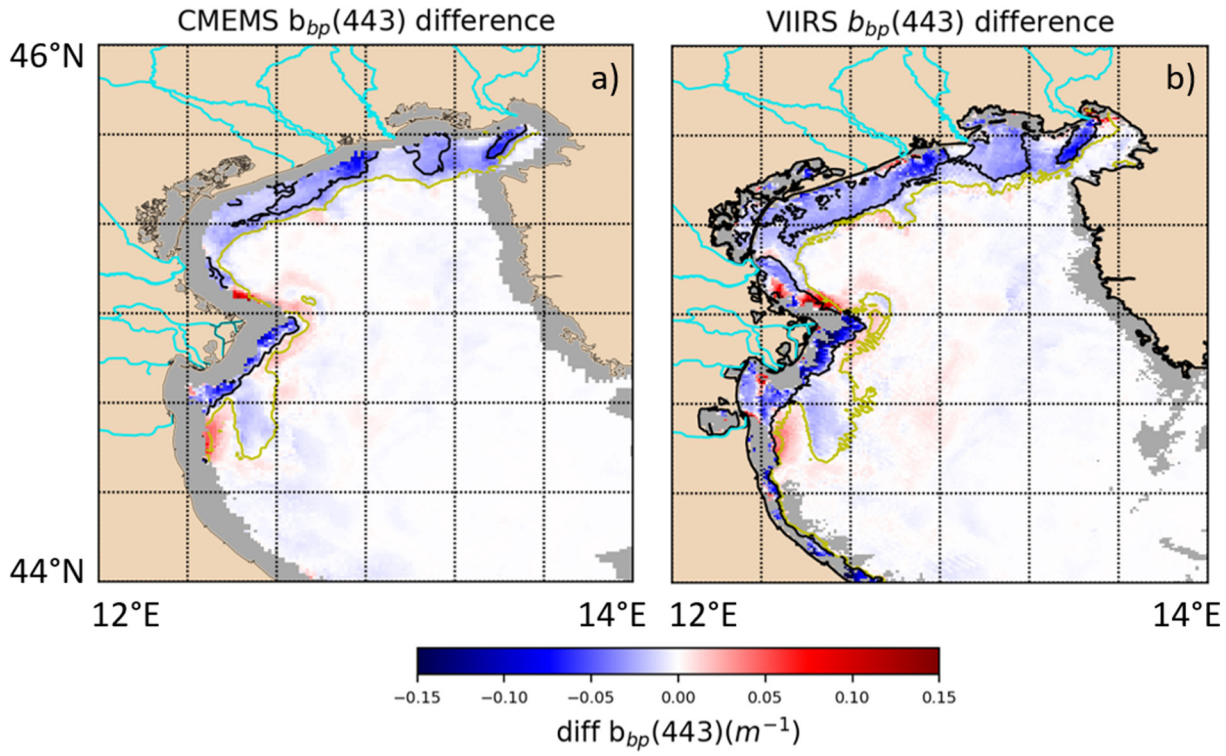

Fig. 11. Analysis of the $b_{bp}(443)$ ~24 h variability. In figure a the difference between the two daily CMEMS $b_{bp}(443)$ images (Fig. 8b minus Fig. 8a, the isolines are those from Fig. 8a). In b the difference between the second VIIRS image of 22nd of March and the first one of 21st of March (Fig. 10b minus Fig. 9a, the isolines are those from Fig. 9a).

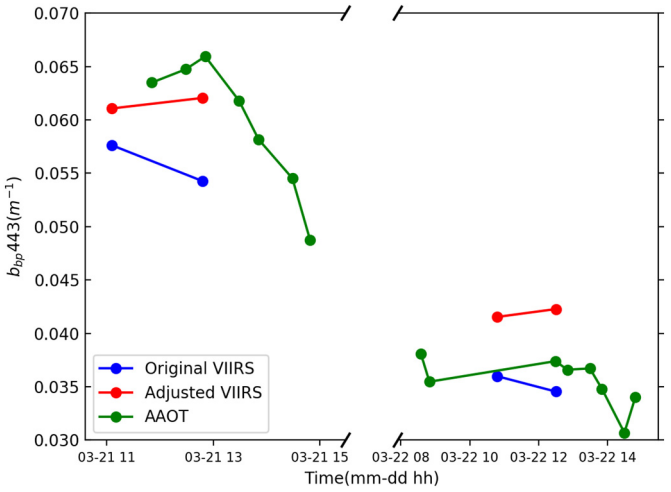

Fig. 12. Analysis of the $b_{bp}(443)$ variability in the AAOT area during 21st and 22nd of March 2013. The green line represents the QAA $b_{bp}(443)$ derived from the AAOT R_{rs}, while the blue and the red line represents the QAA $b_{bp}(443)$ derived from the original and the adjusted VIIRS R_{rs} respectively. (For interpretation of the references to colour in this figure legend, the reader is referred to the web version of this article.)

respectively of −4.1% and 13.1%. During the second day, the original VIIRS $b_{bp}(443)$ shows a better agreement with the in situ observation, than the adjusted one, but the latter seems to better capture the variability. Indeed, the in situ and adjusted VIIRS observations show an increase of this parameter, while the original VIIRS shows a decrease.

4. Summary and future perspective

In this work, the suitability of the adjusted overlapping VIIRS in adequately capture the short time variability of $b_{bp}(443)$ in the NAS was presented. A match-up analysis between the original VIIRS and AAOT R_{rs} data was performed. To the best of our knowledge, there is no literature on the validation of VIIRS in the NAS; nonetheless, the retrieved values of MAPD for MUA1 are very similar to those calculated for MODIS-A and SeaWiFS in previous analyses (Zibordi et al., 2009b; Mélin et al., 2011).

The notable differences, observed between the VIIRS and AAOT R_{rs} for observations performed at SZA > 50°, confirm the results obtained in the work of Barnes and Hu (2016), and that the data acquired at SZA > 60° should be masked. To reduce the dependence of the R_{rs} from the SZA and, consequently, making the HSZ observations available, an adjustment, based on an MLR scheme, was applied, following D'Alimonte et al. (2008). The adjustment brought to a significant improvement of the satellite R_{rs} retrieval. The data at SZA > 50° were those improved the most, and consequently, the HSZ observations were made available in the analysis. This enabled to have a larger number of days (9 of 16) with a full VIIRS overlap, in comparison with the only one almost complete overlap available masking the HSZ observations. Hence, only with the use of those, it is possible to exploit the overlaps of VIIRS to capture short time scale processes in the NAS. Further works should be addressed in the future to reduce the spatial artefacts, observed for pixels acquired at the edge of the swath.

Due to the high uncertainties tied to the QAA $a_{dg}(443)$ retrieval (Lee et al., 2010; Wei and Lee, 2015), the analysis of the short time variability of this IOP was discarded from the study. Different models must be used in the future to retrieve this parameter, starting from the adjusted VIIRS R_{rs} spectrum (Brando et al., 2012; Loisel et al., 2018; Werdell et al., 2013; Werdell et al., 2018). On the contrary, due to the good agreement between the retrieved QAA and the in situ b_{bp} in the NAS (Pitarch et al., 2016), it was possible to analyse its variability.

In the analysed case study, the CMEMS multi daily product, due to its temporal resolution and the applied flags, could detect only the offshore reduction of $b_{bp}(443)$ on a 24 h scale. On the contrary, using the

adjusted overlapping VIIRS, on the first day the coastal and off-shore reduction of $b_{bp}(443)$ was detected, while in the second day a low variability was observed in the northern part. The ~24 h reduction, in the northern part, observed from both CMEMS and VIIRS images was probably due to processes mainly concentrated in few hours during the first day and this was also confirmed by the AAOT observations. The large variability observed in the northern part of the basin during the first day can be attributed to the strong reduction of Livenza and Piave discharges, starting from the 20th of March, and to the settling of the sediment carried by the rivers during the previous days. On the contrary, the tide should not have play a significant role in the $b_{bp}(443)$ dynamics. Indeed, the negligible effect of the tide on sediment transport has been already pointed out in the work of Wang et al. (2007). Furthermore, accordingly to the data acquired at the station of Venezia Puntasalute (Comune di Venezia 2019), a low tidal reduction (respectively 9 and 24 cm) was observed between the two VIIRS images during both days, and this cannot explain the $b_{bp}(443)$ dynamics observed during the case study.

Our work allowed to acquire more information on both temporal and spatial scale in comparison with the CMEMS multi-daily product or other single sensor data. Indeed, by not masking for SL, it was possible to acquire information also for the pixels closest to the shore. Surely, a stricter analysis will be needed in the future to characterize, and eventually reduce, the uncertainties due to the stray-light effect on the previously SL masked data (Bulgarelli et al., 2018).

The approach presented here can be extended to all the middle latitudes coastal areas where an automatic radiometric station representative of the entire basin optical properties is present. It can be also more powerful at high latitudes, where the overlaps are more frequent and more than two images a day may be available.

The use of VIIRS is still insufficient to capture all the $b_{bp}(443)$ variability in the NAS; indeed, the use of this sensor in those areas is limited to hours between 10.30 and 13.00 UTC and no more than two images are available during the same day. Moreover, the presence of clouds and the application of other masks, do not guarantee two full VIIRS images for the days when the overlaps are available.

The work of Mouw et al. (2015) pointed out how only a geostationary sensor, like GOCI, has the needed spatial, temporal and radiometric resolutions to adequately capture the coastal optical variability. The use of multiple observations from different OCR polar orbiting sensors is needed to compensate the absence of a geostationary OCR sensor above different coastal environments, like the NAS, as in this area only the retrieval of Turbidity/SPM is feasible from SEVIRI. Indeed, the exploitation of the VIIRS observations, it is a first step in the creation of a virtual geostationary OCR sensor. The latter, exploiting the multiple images (> 2) provided by the daily observations from different OCR sensors, could allow capturing short time scale events in the coastal areas. The systematic differences between the different OCR sensors can be reduced using the MLR adjustment, used in this work, but in this case the differences between them can be due, not only to the different observation geometries (Barnes and Hu, 2016), but also due to their different processing, and spatial and spectral resolutions. Hence, further considerations should be made on such differences before applying this approach to the different sensors.

Acknowledgments

This work has been performed in the context of the Ocean Colour Thematic Assembly Centre of the Copernicus Marine Environment and Monitoring Service (grant number: 77-CMEMS-TAC-OC) and CoastObs (EU H2020 Grant agreement: 776348). The AERONET Team is acknowledged for the continuous effort in supporting the AERONET-OC sub-network. Giuseppe Zibordi from the Joint Research Center of the European Commission is acknowledged for establishing and maintaining the AAOT AERONET-OC site. Dr. Mario Benincasa, Vega Forneris and Flavio Lapadula from ISMAR-CNR are acknowledged for advice on the implementation of the processing chain. Dr. Marco Bellacicco, Dr. Francesco Bignami, Dr. Davide D'Alimonte, Dr. Davide Dionisi, Dr. Federico Falcini, Dr. Michela Sammartino, and Dr. Giuseppe Zibordi, provided useful comments on earlier versions of this manuscript. We wish to thank the reviewers for the insightful comments.

Description of author's responsibilities

The general conception of this work was developed by MB and VEB. MB, GV, and SC designed and implemented the processing chain. MB and VEB designed the data analysis. MB processed the satellite imagery and performed the data analysis. MB and VEB wrote the manuscript. SC, GV, FB, and RL contributed to the interpretation of the results. All co-authors provided critical comments to the manuscript.

References

Arnone, R.A., Vandermeulen, R.A., Soto, I.M., Ladner, S.D., Ondrusek, M.E., Yang, H., 2017. Diurnal changes in ocean color sensed in satellite imagery. J. Appl. Remote. Sens. 11 (3), 032406.

Babin, M., Morel, A., Fournier-Sicre, V., Fell, F., Stramski, D., 2003a. Light scattering properties of marine particles in coastal and open ocean waters as related to the particle mass concentration. Limnol. Oceanogr. 48 (2), 843–859.

Babin, M., Stramski, D., Ferrari, G.M., Claustre, H., Bricaud, A., Obolensky, G., Hoepffner, N., 2003b. Variations in the light absorption coefficients of phytoplankton, nonalgal particles, and dissolved organic matter in coastal waters around Europe. Journal of Geophysical Research: Oceans (C7), 108.

Barale, V., Jaquet, J.M., Ndiaye, M., 2008. Algal blooming patterns and anomalies in the Mediterranean Sea as derived from the SeaWiFS data set (1998–2003). Remote Sens. Environ. 112 (8), 3300–3313.

Barnes, B.B., Hu, C., 2016. Dependence of satellite ocean color data products on viewing angles: a comparison between SeaWiFS, MODIS, and VIIRS. Remote Sens. Environ. 175, 120–129.

Barnes, B.B., Cannizzaro, J.P., English, D.C., Hu, C., 2019. Validation of VIIRS and MODIS reflectance data in coastal and oceanic waters: an assessment of methods. Remote Sens. Environ. 220, 110–123.

Bignami, F., Sciarra, R., Carniel, S., Santoleri, R., 2007. Variability of Adriatic Sea coastal turbid waters from SeaWiFS imagery. Journal of Geophysical Research: Oceans (C3), 112.

Blondeau-Patissier, D., Brando, V.E., Oubelkheir, K., Dekker, A.G., Clementson, L.A., Daniel, P., 2009. Bio-optical variability of the absorption and scattering properties of the Queensland inshore and reef waters, Australia. Journal of Geophysical Research: Oceans (C5), 114.

Boldrin, A., Carniel, S., Giani, M., Marini, M., Bernardi Aubry, F., Campanelli, A., Russo, A., 2009. Effects of bora wind on physical and biogeochemical properties of stratified waters in the northern Adriatic. Journal of Geophysical Research: Oceans (C8), 114.

Bouali, M., Ignatov, A., 2014. Adaptive reduction of striping for improved sea surface temperature imagery from Suomi National Polar-Orbiting Partnership (S-NPP) visible infrared imaging radiometer suite (VIIRS). J. Atmos. Ocean. Technol. 31 (1), 150–163.

Braga, F., Zaggia, L., Bellafiore, D., Bresciani, M., Giardino, C., Lorenzetti, G., Brando, V.E., 2017. Mapping turbidity patterns in the Po river prodelta using multi-temporal Landsat 8 imagery. Estuar. Coast. Shelf Sci. 198, 555–567.

Brando, V.E., Dekker, A.G., Park, Y.J., Schroeder, T., 2012. Adaptive semianalytical inversion of ocean color radiometry in optically complex waters. Appl. Opt. 51 (15), 2808–2833.

Brando, V.E., Braga, F., Zaggia, L., Giardino, C., Bresciani, M., Matta, E., Bonaldo, D., 2015. High-resolution satellite turbidity and sea surface temperature observations of river plume interactions during a significant flood event. Ocean Sci. 11 (6), 909–920.

Bulgarelli, B., Zibordi, G., Mélin, F., 2018. On the minimization of adjacency effects in SeaWiFS primary data products from coastal areas. Opt. Express 26 (18), A709–A728.

Cao, C., Xiong, X., Wolfe, R., De Luccia, F., Liu, Q., Blonski, S., … & Hillger, D. (2013). Visible Infrared Imaging Radiometer Suite (VIIRS) Sensor Data Record (SDR) User's Guide. NOAA Technical Report NESDIS: College Park, MD, USA.

Cao, C., De Luccia, F.J., Xiong, X., Wolfe, R., Weng, F., 2014. Early on-orbit performance of the visible infrared imaging radiometer suite onboard the Suomi National Polar-Orbiting Partnership (S-NPP) satellite. IEEE Trans. Geosci. Remote Sens. 52 (2), 1142–1156.

Choi, J.K., Park, Y.J., Ahn, J.H., Lim, H.S., Eom, J., Ryu, J.H., 2012. GOCI, the world's first geostationary ocean color observation satellite, for the monitoring of temporal variability in coastal water turbidity. Journal of Geophysical Research: Oceans 117 (C9).

Choi, J.K., Park, Y.J., Lee, B.R., Eom, J., Moon, J.E., Ryu, J.H., 2014. Application of the Geostationary Ocean Color Imager (GOCI) to mapping the temporal dynamics of coastal water turbidity. Remote Sens. Environ. 146, 24–35.

Collins, M.B., Balson, P.S., 2007. Coastal and shelf sediment transport: an introduction. Geol. Soc. Lond., Spec. Publ. 274 (1), 1–5.

Concha, J., Mannino, A., Franz, B., Kim, W., 2019. Uncertainties in the Geostationary Ocean Color Imager (GOCI) remote sensing reflectance for assessing diurnal

variability of biogeochemical processes. Remote Sens. 11 (3), 295.
Cozzi, S., Giani, M., 2011. River water and nutrient discharges in the Northern Adriatic Sea: current importance and long term changes. Cont. Shelf Res. 31 (18), 1881–1893.
D'Alimonte, D., Zibordi, G., Melin, F., 2008. A statistical method for generating cross-mission consistent normalized water-leaving radiances. IEEE Trans. Geosci. Remote Sens. 46 (12), 4075–4093.
Degobbis, D., Precali, R., Ivancic, I., Smodlaka, N., Fuks, D., Kveder, S., 2000. Long-term changes in the northern Adriatic ecosystem related to anthropogenic eutrophication. Int. J. Environ. Pollut. 13 (1–6), 495–533.
Dogliotti, A.I., Ruddick, K., Guerrero, R., 2016. Seasonal and inter-annual turbidity variability in the Río de la Plata from 15 years of MODIS: El Niño dilution effect. Estuar. Coast. Shelf Sci. 182, 27–39.
Drusch, M., Del Bello, U., Carlier, S., Colin, O., Fernandez, V., Gascon, F., Meygret, A., 2012. Sentinel-2: ESA's optical high-resolution mission for GMES operational services. Remote Sens. Environ. 120, 25–36.
Duan, H., Ma, R., Loiselle, S.A., Shen, Q., Yin, H., Zhang, Y., 2014. Optical characterization of black water blooms in eutrophic waters. Sci. Total Environ. 482, 174–183.
Eplee, R.E., Meister, G., Patt, F.S., Barnes, R.A., Bailey, S.W., Franz, B.A., McClain, C.R., 2012. On-orbit calibration of SeaWiFS. Appl. Opt. 51 (36), 8702–8730.
Falcieri, F.M., Benetazzo, A., Sclavo, M., Russo, A., Carniel, S., 2014. Po River plume pattern variability investigated from model data. Cont. Shelf Res. 87, 84–95.
Falcini, F., Khan, N.S., Macelloni, L., Horton, B.P., Lutken, C.B., McKee, K.L., D'Emidio, M., 2012. Linking the historic 2011 Mississippi River flood to coastal wetland sedimentation. Nat. Geosci. 5 (11), 803.
Fernández-Nóvoa, D., Gómez-Gesteira, M., Mendes, R., Vaz, N., Dias, J.M., 2017. Influence of main forcing affecting the Tagus turbid plume under high river discharges using MODIS imagery. PLoS One 12 (10), e0187036.
Ganju, N. K., Miselis, J. L., & Aretxabaleta, A. L. (2014). Physical and biogeochemical controls on light attenuation in a eutrophic, back-barrier estuary.
Gernez, P., Doxaran, D., Barillé, L., 2017. Shellfish aquaculture from space: potential of Sentinel2 to monitor tide-driven changes in turbidity, chlorophyll concentration and oyster physiological response at the scale of an oyster farm. Front. Mar. Sci. 4, 137.
Harris, C.K., Sherwood, C.R., Signell, R.P., Bever, A.J., Warner, J.C., 2008. Sediment dispersal in the northwestern Adriatic Sea. Journal of Geophysical Research: Oceans (C11), 113.
Hestir, E.L., Brando, V.E., Bresciani, M., Giardino, C., Matta, E., Villa, P., Dekker, A.G., 2015. Measuring freshwater aquatic ecosystems: the need for a hyperspectral global mapping satellite mission. Remote Sens. Environ. 167, 181–195.
Holben, B.N., Eck, T.F., Slutsker, I., Tanre, D., Buis, J.P., Setzer, A., Lavenu, F., 1998. AERONET—a federated instrument network and data archive for aerosol characterization. Remote Sens. Environ. 66 (1), 1–16.
Kaufman, Y.J., 1984. Atmospheric effect on spatial resolution of surface imagery. Appl. Opt. 23 (19), 3400–3408.
Le, C., Hu, C., English, D., Cannizzaro, J., Chen, Z., Feng, L., Kovach, C., 2013. Towards a long-term chlorophyll-a data record in a turbid estuary using MODIS observations. Prog. Oceanogr. 109, 90–103.
Lee, Z., Carder, K.L., Arnone, R.A., 2002. Deriving inherent optical properties from water color: a multiband quasi-analytical algorithm for optically deep waters. Appl. Opt. 41 (27), 5755–5772.
Lee, Z., Arnone, R., Hu, C., Werdell, P.J., Lubac, B., 2010. Uncertainties of optical parameters and their propagations in an analytical ocean color inversion algorithm. Appl. Opt. 49 (3), 369–381.
Lee, Z.P., Du, K., Voss, K.J., Zibordi, G., Lubac, B., Arnone, R., Weidemann, A., 2011. An inherent-optical-property-centered approach to correct the angular effects in water-leaving radiance. Appl. Opt. 50 (19), 3155–3167.
Lee, ZhongPing, Carder, Kendall L., Arnone, Robert A., 2014. Quasi-Analytical Algorithm v6 Update. http://www.ioccg.org/groups/Software_OCA/QAA_v6_2014209.pdf.
Loisel, H., Bosc, E., Stramski, D., Oubelkheir, K., Deschamps, P.Y., 2001. Seasonal variability of the backscattering coefficient in the Mediterranean Sea based on satellite SeaWiFS imagery. Geophys. Res. Lett. 28 (22), 4203–4206.
Loisel, H., Stramski, D., Dessailly, D., Jamet, C., Li, L., Reynolds, R.A., 2018. An inverse model for estimating the optical absorption and backscattering coefficients of seawater from remote-sensing reflectance over a broad range of oceanic and coastal marine environments. Journal of Geophysical Research: Oceans 123 (3), 2141–2171.
Malačič, V., Viezzoli, D., Cushman-Roisin, B., 2000. Tidal dynamics in the northern Adriatic Sea. Journal of Geophysical Research: Oceans 105 (C11), 26265–26280.
Manzo, C., Federica, B., Luca, Z., Ernesto, B.V., Claudia, G., Mariano, B., Cristiana, B., 2018. Spatio-temporal analysis of prodelta dynamics by means of new satellite generation: the case of Po river by Landsat-8 data. Int. J. Appl. Earth Obs. Geoinf. 66, 210–225.
Marini, M., Jones, B.H., Campanelli, A., Grilli, F., Lee, C.M., 2008. Seasonal variability and Po River plume influence on biochemical properties along western Adriatic coast. Journal of Geophysical Research: Oceans (C5), 113.
Mélin, F., Sclep, G., 2015. Band shifting for ocean color multi-spectral reflectance data. Opt. Express 23 (3), 2262–2279.
Mélin, F., Vantrepotte, V., Clerici, M., D'Alimonte, D., Zibordi, G., Berthon, J.F., Canuti, E., 2011. Multi-sensor satellite time series of optical properties and chlorophyll-a concentration in the Adriatic Sea. Prog. Oceanogr. 91 (3), 229–244.
Mikelsons, K., Wang, M., Jiang, L., Bouali, M., 2014. Destriping algorithm for improved satellite-derived ocean color product imagery. Opt. Express 22 (23), 28058–28070.
Morel, A., Mueller, J.L., 2002. Normalized water-leaving radiance and remote sensing reflectance: Bidirectional reflectance and other factors. In: Ocean Optics Protocols for Satellite Ocean Color Sensor Validation. vol. 2. pp. 183–210.
Morel, A., Voss, K.J., Gentili, B., 1996. Bidirectional reflectance of oceanic waters: a comparison of modeled and measured upward radiance fields. Oceanogr. Lit. Rev. 2 (43), 108.
Morel, A., Antoine, D., Gentili, B., 2002. Bidirectional reflectance of oceanic waters: accounting for Raman emission and varying particle scattering phase function. Appl. Opt. 41 (30), 6289–6306.
Mouw, C.B., Greb, S., Aurin, D., DiGiacomo, P.M., Lee, Z., Twardowski, M., Moses, W., 2015. Aquatic color radiometry remote sensing of coastal and inland waters: challenges and recommendations for future satellite missions. Remote Sens. Environ. 160, 15–30.
NASA Goddard Space Flight Center, Ocean Ecology Laboratory, Ocean Biology Processing Group, 2018. Visible and Infrared Imager/Radiometer Suite (VIIRS) Ocean Color Data. Reprocessing. NASA OB.DAAC, Greenbelt, MD, USA. https://doi.org/10.5067/JPSS1/VIIRS/L2/OC/2018. (Accessed on 11/15/2018).
Neukermans, G., Ruddick, K., Bernard, E., Ramon, D., Nechad, B., Deschamps, P.Y., 2009. Mapping total suspended matter from geostationary satellites: a feasibility study with SEVIRI in the Southern North Sea. Opt. Express 17 (16), 14029–14052.
Neukermans, G., Ruddick, K.G., Greenwood, N., 2012. Diurnal variability of turbidity and light attenuation in the southern North Sea from the SEVIRI geostationary sensor. Remote Sens. Environ. 124, 564–580.
Pahlevan, N., Sheldonc, P., Peric, F., Weic, J., Shangc, Z., Sunc, Q., Lovelande, T., 2016a. Calibration/validation of Landsat-derived ocean colour products in Boston harbour. International Archives of the Photogrammetry. Remote Sensing and Spatial Information Sciences 8.
Pahlevan, N., Sarkar, S., Franz, B.A., 2016b. Uncertainties in coastal ocean color products: impacts of spatial sampling. Remote Sens. Environ. 181, 14–26.
Pitarch, J., Bellacicco, M., Volpe, G., Colella, S., Santoleri, R., 2016. Use of the quasi-analytical algorithm to retrieve backscattering from in-situ data in the Mediterranean Sea. Remote Sensing Letters 7 (6), 591–600.
Qi, L., Hu, C., Barnes, B.B., Lee, Z., 2017. VIIRS captures phytoplankton vertical migration in the NE Gulf of Mexico. Harmful Algae 66, 40–46.
Roy, D.P., Wulder, M.A., Loveland, T.R., Woodcock, C.E., Allen, R.G., Anderson, M.C., ... Scambos, T.A., 2014. Landsat-8: science and product vision for terrestrial global change research. Remote Sens. Environ. 145, 154–172.
Ruddick, K., Vanhellemont, Q., Yan, J., Neukermans, G., Wei, G., Shang, S., 2012. Variability of suspended particulate matter in the Bohai Sea from the Geostationary Ocean Color Imager (GOCI). Ocean Science Journal 47 (3), 331–345.
Ruddick, K., Neukermans, G., Vanhellemont, Q., Jolivet, D., 2014. Challenges and opportunities for geostationary ocean colour remote sensing of regional seas: a review of recent results. Remote Sens. Environ. 146, 63–76.
Ryu, J.H., Han, H.J., Cho, S., Park, Y.J., Ahn, Y.H., 2012. Overview of geostationary ocean color imager (GOCI) and GOCI data processing system (GDPS). Ocean Science Journal 47 (3), 223–233.
Schmid, J., 2000, May. The SEVIRI instrument. In: Proceedings of the 2000 EUMETSAT Meteorological Satellite Data User's Conference, Bologna, Italy. vol. 29.
Schroeder, T., Devlin, M.J., Brando, V.E., Dekker, A.G., Brodie, J.E., Clementson, L.A., McKinna, L., 2012. Inter-annual variability of wet season freshwater plume extent into the Great Barrier Reef lagoon based on satellite coastal ocean colour observations. Mar. Pollut. Bull. 65 (4–9), 210–223.
Solidoro, C., Bastianini, M., Bandelj, V., Codermatz, R., Cossarini, G., Canu, D.M., ... Trevisani, S., 2009. Current state, scales of variability, and trends of biogeochemical properties in the northern Adriatic Sea. Journal of Geophysical Research: Oceans (C7), 114.
Sterckx, S., Knaeps, E., Ruddick, K., 2011. Detection and correction of adjacency effects in hyperspectral airborne data of coastal and inland waters: the use of the near infrared similarity spectrum. Int. J. Remote Sens. 32 (21), 6479–6505.
Van Mol, B., Ruddick, K., 2005, March. Total suspended matter maps from CHRIS imagery of a small inland water body in Oostende (Belgium). In: Proceedings of the 3rd ESA CHRIS/Proba Workshop, pp. 21–23.
Volpe, G., Colella, S., Brando, V.E., Forneris, V., La Padula, F., Di Cicco, A., Sammartino, M., Bracaglia, M., Artuso, F., Santoleri, R., 2019. Mediterranean ocean colour Level 3 operational multi-sensor processing. Ocean Sci. 15, 127–146. https://doi.org/10.5194/os-15-127-2019.
Wang, X.H., Pinardi, N., 2002. Modeling the dynamics of sediment transport and resuspension in the northern Adriatic Sea. Journal of Geophysical Research: Oceans 107 (C12).
Wang, X.H., Pinardi, N., Malacic, V., 2007. Sediment transport and resuspension due to combined motion of wave and current in the northern Adriatic Sea during a Bora event in January 2001: a numerical modelling study. Cont. Shelf Res. 27 (5), 613–633.
Wang, M., Son, S., Jiang, L., Shi, W., 2014. Observations of ocean diurnal variations from the Korean geostationary ocean color imager (GOCI). In: Ocean Sensing and Monitoring VI. vol. 9111. International Society for Optics and Photonics, pp. 911102.
Wei, J., Lee, Z., 2015. Retrieval of phytoplankton and colored detrital matter absorption coefficients with remote sensing reflectance in an ultraviolet band. Appl. Opt. 54 (4), 636–649.
Werdell, P.J., Franz, B.A., Bailey, S.W., Feldman, G.C., Boss, E., Brando, V.E., Loisel, H., 2013. Generalized ocean color inversion model for retrieving marine inherent optical properties. Appl. Opt. 52 (10), 2019–2037.
Werdell, P.J., McKinna, L.I., Boss, E., Ackleson, S.G., Craig, S.E., Gregg, W.W., Stramski, D., 2018. An overview of approaches and challenges for retrieving marine inherent optical properties from ocean color remote sensing. Prog. Oceanogr. 160, 186–212.
Zavatarelli, M., Raicich, F., Bregant, D., Russo, A., Artegiani, A., 1998. Climatological biogeochemical characteristics of the Adriatic Sea. J. Mar. Syst. 18 (1–3), 227–263.
Zibordi, G., Hooker, S.B., Berthon, J.F., D'Alimonte, D., 2002. Autonomous above-water radiance measurements from an offshore platform: a field assessment experiment. J. Atmos. Ocean. Technol. 19 (5), 808–819.
Zibordi, G., Holben, B., Hooker, S.B., Mélin, F., Berthon, J.F., Slutsker, I., Schuster, G.,

2006. A network for standardized ocean color validation measurements. Eos, Transactions American Geophysical Union 87 (30), 293–297.
Zibordi, G., Mélin, F., Berthon, J.F., Holben, B., Slutsker, I., Giles, D., Fabbri, B.E., 2009a. AERONET-OC: a network for the validation of ocean color primary products. J. Atmos. Ocean. Technol. 26 (8), 1634–1651.
Zibordi, G., Berthon, J.F., Mélin, F., D'Alimonte, D., Kaitala, S., 2009b. Validation of satellite ocean color primary products at optically complex coastal sites: Northern Adriatic Sea, Northern Baltic Proper and Gulf of Finland. Remote Sens. Environ. 113 (12), 2574–2591.

Web references

Python, 2019c. https://scikit-learn.org/stable/modules/generated/sklearn.linear_model.LinearRegression.html.
ARPAE, 2019. https://www.arpae.it/sim/, Accessed date: 16 February 2019.
ARPAV, 2019. http://www.arpa.veneto.it/temi-ambientali/idrologia/file-e-allegati/rapporti-e-documenti/idrologia-regionale/idrologia-regionale-la-rete-idrometrica, Accessed date: 16 February 2019.
Comune di Venezia https://www.comune.venezia.it/it/content/archivio-storico-livello-marea-venezia-1, Accessed date: 28 May 2019.
NASA, 2019. https://oceancolor.gsfc.nasa.gov/atbd/ocl2flags/, Accessed date: 16 February 2019.
NASA, 2019b. https://aeronet.gsfc.nasa.gov/new_web/ocean_color.html, Accessed date: 16 February 2019.
NASA, 2019c. https://oceandata.sci.gsfc.nasa.gov/VIIRS-SNPP/L1/, Accessed date: 16 February 2019.
Python, 2019. https://pypi.org/project/pyproj/, Accessed date: 16 February 2019.
Python, 2019b. https://pyresample.readthedocs.io/en/stable/, Accessed date: 16 February 2019.